Design and Optimization of Low-Frequency Piezoelectric MEMS Energy Harvesters Based on Machine Learning

By
©Hamidreza Ehsani Chimeh

A dissertation submitted to the School of Graduate Studies
in partial fulfillment of the requirements for the degree of

Master of Engineering

Faculty of Engineering & Applied Science
Memorial University of Newfoundland

Supervisory Committee

Dr. Lihong Zhang (Co-supervisor)
Dr. Mohammad Al Janaideh (Co-Supervisor)

February 2022

St. John's, Newfoundland

Abstract

Portable electronic applications are typically powered by batteries, which have limited lifespan and size constraints. Energy harvesting from parasitic vibrations using piezoelectricity is a demanding solution to improving the power supply efficiency of low-power portable devices and autonomous sensor networks. Vibrational energy harvesters with high operating frequency are not desirable considering the low-frequency characteristics of ambient vibrations (e.g., wind). The operation frequency range (known as bandwidth) is a key feature that should be improved under an unpredictable or uncontrollable condition of ambient vibrations. In this thesis, several piezoelectric MEMS energy harvesters have been developed to tackle these challenges.

In order to facilitate the design process and determine the optimum physical dimensions, an artificial neural network is used to model the designs. In the first step, a sample dataset is created by numerical modeling to train a deep neural network. The validation results indicate that the trained DNN model can achieve around 90% estimation accuracy of device features, such as resonant frequency and harvested voltage. Next, this trained model is integrated with genetic algorithm as a performance estimator to optimize the geometry of the harvester to lower the resonant frequencies and improve the harvested voltage.

With the intention of improving the accuracy of deep neural network, the transfer learning method is used for modeling another design. In this method, the DNN is firstly trained with a dataset created by the lump-parameter model; then, the trained network is transferred to a new deep model for another round of training with highly accurate FEM data samples to further reduce prediction error. It was shown that the new model can estimate the device features with more than 94% accuracy, which is 4% higher than the regular DNN. Finally, in the last design, our proposed AI-based methodology is utilized to estimate the mode shapes to enlarge the operational bandwidth specifically. The optimized energy harvesters have been fabricated through a standard micromachining process. Our measurement results confirm that the proposed AI-based methods can help reach the balanced summit of higher power density, lower resonant frequency, and larger bandwidth among the published works.

Acknowledgments

I would like to express my sincere gratitude to my supervisors Dr. Lihong Zhang and Dr. Mohammad Al Janaideh for their continuous support in my master's study, research, motivation, enthusiasm, immense knowledge and their assistance in writing papers and thesis. This work was supported in part by the Natural Sciences and Engineering Research Council of Canada, in part by Canada Foundation for Innovation, in part by the Research and Development Corporation of Newfoundland and Labrador, in part by Memorial University of Newfoundland, and in part by CMC Microsystems.

To the loving memory of my grandparents

Table of Contents

List of Tables

List of Figures

List of Abbreviations

Microelectromechanical Systems	**MEMS**
Deep Neural Network	**DNN**
Genetic Algorithm	**GA**
Finite Element Modeling	**FEM**
Scanning Electron Microscope	**SEM**
Maximum Power Point Tracking	**MPPT**
Synchronized Switch Harvesting on Inductor	**SSHI**
Synchronous Electric Charge Extraction	**SECE**
Convolutional Neural Network	**CNN**
Solid Isotropic Material with Penalization	**SIMP**
Fast Fourier Transform	**FFT**
Artificial Neural Network	**ANN**

Chapter 1 Introduction

Energy harvesting from renewable energy sources such as wind, solar, hydro, geothermal, and biomass energy has been significantly improved during the past years. However, up to now fossil fuels are still producing more than 80% of the total global energy [1], which somehow exhibits a likely long journey for the alternative energy resources especially renewable energy to go in order to meet the future demand and completely resolve the environmental concerns. There is no doubt that more clean energy sources are being explored, and this research is also an effort in the same direction. Other clean energy sources include hydrogen, nuclear fusion energy with no hazardous waste, offshore wind, and even next-generation space power technologies, all of which are currently developing [2]. Many efforts have been made to reduce or eliminate the adverse impacts of natural energy sources on the surrounding environment. Besides natural energy sources, energy harvesting is another solution to providing sustainable power supplies without lifetime concerns.

If low-power low-voltage small electronic devices such as wireless sensor networks for environmental monitoring are located in remote inaccessible regions, providing sustainable power supplies is highly demanded. Energy harvesting can also provide a solution to harsh environmental conditions where using batteries is impractical. The batteries, which operate by using the chemical energy stored inside, must be sufficiently robust to survive anticipated environmental conditions. There should be minimal electrolyte leakage, which may take place during severe short-circuit environments. Particulate ingress, extreme temperature, physical impact, electrostatic discharge (ESD), electromagnetic interference (EMI), and extreme vibration may form the harsh environmental conditions, which, if unchecked in advance, will readily destroy batteries over time. Moreover, batteries are very polluting environmentally considering the heavy metals like lead and cadmium used inside. Hence, cleaner alternatives are being actively pursued.

Capturing energy from ubiquitous parasitic vibrations has become more appealing for small-scale applications among various renewable energy sources such as solar or thermal energy [3]. Unused vibration may be produced by human activities, vehicles, wind, or other environmental movements [4]. For converting vibration energy to electricity, the techniques based on electrostatic, electromagnetic, triboelectric, and piezoelectricity are among the most feasible ones. Many aspects of these techniques have been intensively studied in the literature for MEMS scale design. For example, in electromagnetic converters, a bulky magnet is usually required to achieve high efficiency [5]. Therefore, this approach would not fit into small scale (i.e., less than ~0.5cm^3) applications, and the portability feature may not be easily achieved. Compared to others, energy conversion

based on piezoelectricity features higher power density and better compatibility with micromachining fabrication process.

Micro-Electro-Mechanical Systems (MEMS) is a miniaturized combination of mechanical and electronic parts, typically with dimensions less than one millimeter, which are made by using specific microfabrication techniques. MEMS technology was first introduced in the 1960s [6], and it has significantly changed the way of designing sensors and actuators. The advantages of MEMS devices include low power consumption, flexibility, compatibility, fast integration, transportability, and low thermal constant. MEMS devices are widely used for either sensing or actuation. In this thesis, we will explore the concept of producing energy from vibrations in MEMS devices, which involves piezoelectric materials for energy conversion, as one of the most energy-dense sources among alternatives.

In this thesis, we have developed three piezoelectric MEMS vibration energy harvesters. Moreover, a design automation methodology based on deep artificial neural network and genetic algorithm has been proposed to obtain optimal geometry of energy harvesters. The first design presents a serpentine-shaped structure with a low resonant frequency, which is optimized by our proposed optimization method to improve the power capturing efficiency and reduce the operation frequency. As for the second energy harvester, a new transfer learning technique is used to enhance the performance of our optimization method for a bi-stable structure. Finally, in the last work, a new multimode structure is designed to further improve the efficiency of the harvester in terms of operational bandwidth.

The rest of the thesis is structured as follows. Chapter 2 reviews the basics and previous works in vibration-based energy harvesting. In Chapter 3, a piezoelectric MEMS energy harvester with the capability of operating at a low resonant frequency (i.e., less than 200 Hz) is proposed. Chapter 4 presents a transfer-learning-based optimization methodology to enhance the performance of an M-shaped energy harvester. A new structure with wideband operation is discussed in Chapter 5. In Chapter 6 we draw a conclusion and point out future works for this research.

Chapter 2 Fundamentals and Literature Review

2.1. Piezoelectric Energy Harvesting

The piezoelectric material is able to convert mechanical stress into an electrical charge, which is termed a direct piezoelectric effect. The piezoelectric material can also transform electrical charge into mechanical stress, called the converse piezoelectric effect. The combination of the actuation strain caused by the applied electric voltage and mechanical strain from mechanical stress forms the total strain. Fig. 1 shows the principle working of piezoelectric material, and the well-known constitutive equation describing the characteristics of a piezoelectric material can be given by [7]:

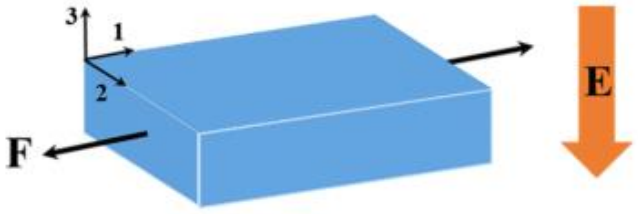

Fig. 1. Piezoelectric transducer

$$S_1 = s_{11}^E T_1 + d_{31} E_3 \,, \quad (1)$$

$$D_3 = d_{31} T_1 + \varepsilon_{33}^T E_3 \,, \quad (2)$$

where S_1 is the strain, T_1 is the stress, D_3 is the charge density, E_3 is the electric field, d_{31} is the piezoelectric constant, s_{11}^E is the mechanical compliance at constant electric field, and ε_{33}^T is the permittivity at constant stress. The index numbers represent the directions relative to the polar axis. Two common coupling modes for piezoelectric transducers are displayed in Fig. 2. In d_{33} mode, the direction of applied stress is parallel to the polar axis, while in d_{31} mode, they are perpendicular to each other.

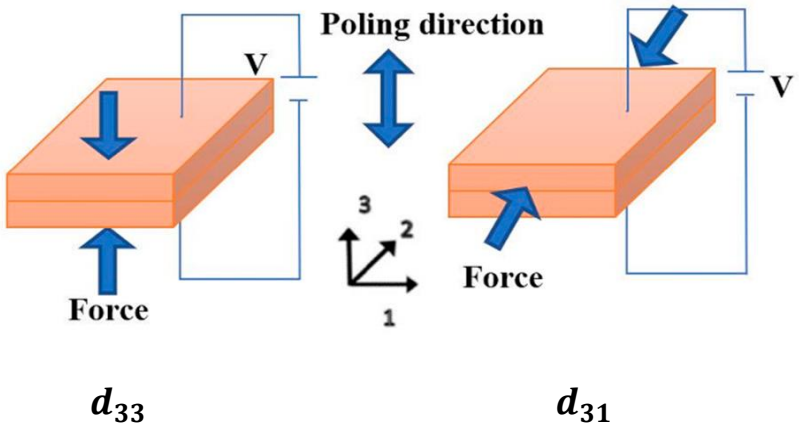

Fig. 2. Two modes of piezoelectric material [8]

The conventional MEMS energy harvesters typically use a single straight cantilever clamped at one end and a proof mass at the tip free part of the other end to collect ambient vibrations. The piezoelectric materials can be deposited either on one side of the cantilever, called unimorph configuration, or on both sides, called bimorph configuration [9]. This

commonly used structure can be modeled as a single degree of freedom lumped spring-mass system [10]. So, the equation of motion can be expressed as:

$$m\ddot{z}(t) + b\dot{z}(t) + kz(t) = -ma(t) . \quad (3)$$

By using Laplace transform, the transfer function of the system could be obtained as:

$$\frac{z(s)}{a(s)} = \frac{1}{s^2+\frac{b}{m}s+\frac{k}{m}} = \frac{1}{s^2+\omega_n Q s+{\omega_n}^2} , \quad (4)$$

where ω_n is the natural frequency of the system, and Q is the quality factor. Thus, the resonant frequency of the system can be written as:

$$f_n = \frac{1}{2\pi}\sqrt{\frac{k}{m}} , \quad (5)$$

where k is the bending stiffness and m is the effective mass. The maximum deflection and energy conversion occurs when the applied vibration is close to the resonance frequency. A few deviations from resonance frequency results in a significant power loss. Although these types of harvesters are easy to model and build, they usually have high natural frequency and narrow bandwidth, which may not be desirable for a real environment with vibrations normally in a low-frequency range. Recently several approaches have been proposed to improve the frequency features of energy harvesters.

2.2. Previous Works

One common way to reduce the operational frequency is to add large proof masses into the cantilever [11]. Another feasible solution is to increase the effective surface area of cantilever by using a spiral structure. Song *et al*. [12] showed that the natural frequency of spiral energy harvesters could be reduced by increasing the number of spiral turns. However, in this design the power efficiency gradually decreases after five turns due to torsion, which becomes dominant in the first mode of vibration, and voltage cancellation occurs as a result. The output peak voltage of this harvester is shown in Fig. 3

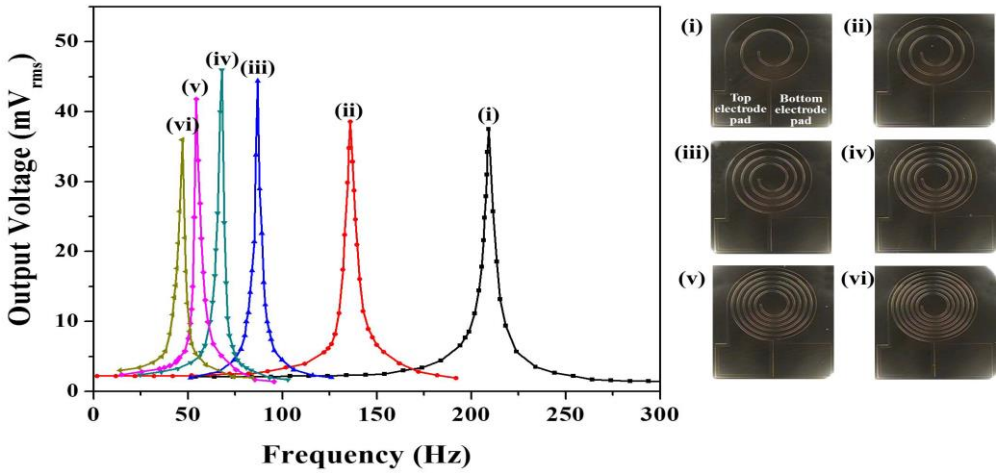

Fig. 3. Frequency response of spiral designs with various number of turns

Apo *et al.* [13] developed several arc-based harvesters without any additional masses in the zigzag or simple straight structure, which are displayed in Fig. 4. The cantilevers are formed by a series of S-shaped segments dominating the bending mode as the first natural frequency of the devices. The experimental results confirm that the arc-based harvesters can resonate at significantly lower frequencies than their linear counterparts and exhibit

less torsion than the spiral designs. Sharpes *et al.* [14] also investigated the performance of the zigzag-shaped structure in comparison to flex and elephant structures in terms of low-frequency feature and electromechanical coupling. They have shown that the elephant-shaped harvester can hold more power density than the other two devices, due to elimination of the torsional effect. Nevertheless, the amount of the reported harvested power is relatively small especially considering the fact that the design is not exactly fitted into the regular MEMS scale.

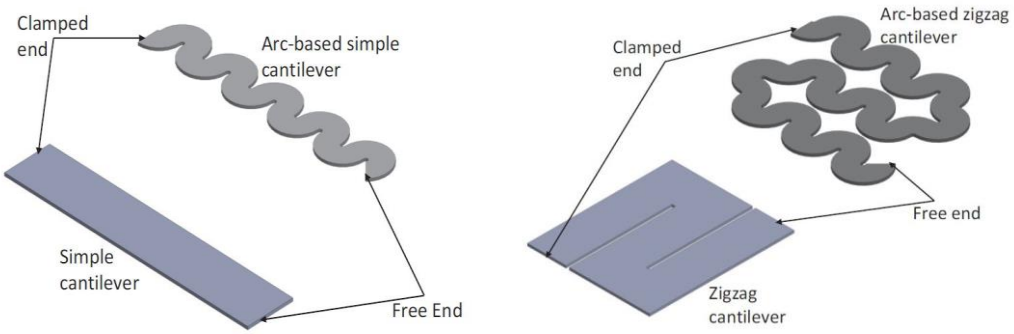

Fig. 4. Arc-based energy harvesters

Another well-known approach to reduce the operational frequency range is based on magnet or impact method (called frequency up-conversion technique) by using stoppers. For instance, Dechant *et al.* [15] placed two stoppers as impact members at both sides of the disc-shaped energy harvester with a proof mass in the middle. Under the shock excitation, the stoppers make contact with the diaphragm and limit the device oscillation. As a result, the system undergoes an impulse reaction and starts to vibrate at its own resonant frequency. In such a setting, the oscillation is transferred to a high frequency (i.e., 340 Hz), although energy dissipation and even damage may occur due to impact.

In order to expand the bandwidth of energy harvesters, researchers have proposed distinct techniques, including integration of multiple cantilever beams or irregular geometries with different mode shapes, frequency tuning, and nonlinear method [16][17][18][19]. For the first technique, multiple resonant frequencies are generated by adding degrees-of-freedom [20][21] or applying generator arrays to broaden the harvesting bandwidth [22]. As for the frequency tuning technique, magnets may be used as a non-contact mechanism to change the axial tension of the beam. For example, a two degrees of freedom energy harvester was introduced by Wang and Tang in [23] with magnetic coupling. In this work, a parasitic oscillator is attached to the main beam to get the second resonant mode, and the magnet is used to impose nonlinear force at the tip part. Although their results indicate an increase in bandwidth by 10 Hz, the magnetic force requires high-level excitation for this type of harvesters to operate effectively. Moreover, a magnetic-based setting makes the device fabrication complicated for the MEMS micromachining process. In [20][19], Nabavi and Zhang developed a piezoelectric MEMS harvester by using the nonlinear method. Although the boosted bandwidth is considerable, the operational frequencies are relatively higher and the magnitude of the harvested voltage is fairly limited.

2.3. Power Management Circuit

Efficient power transfer from the piezoelectric device to the load is another area to be studied in energy harvesting. Since energy harvesters usually have low output power, it is essential to use a power management circuit to provide efficient AC-DC conversion and

voltage regulation. The first stage of AC-DC conversion is full-wave rectification; however, the conventional full-bridge rectifier could not be effective enough due to the voltage drop across the diodes. One way to overcome this issue is to use a gate cross-coupled or fully cross-coupled configuration with an ultra-low threshold voltage (i.e., zero-threshold voltage) MOSFETs [24]. Another approach to reducing the voltage drop barrier is to use active rectification. Fig. 5 displays the schematic of an active diode based on comparator, which is equivalent to an ideal diode. This configuration almost performs with no forward voltage drop and perfectly block the reverse current.

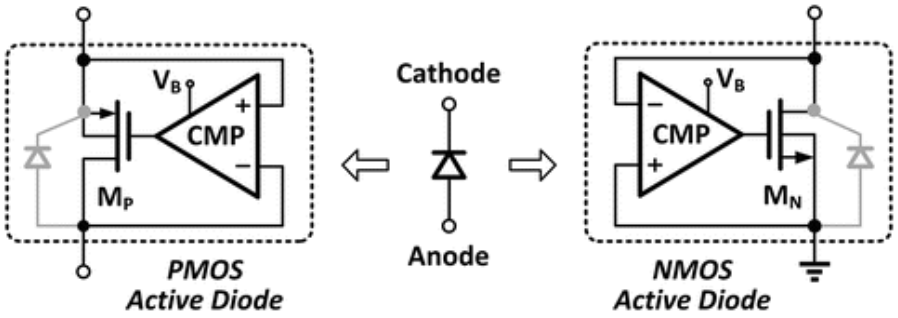

Fig. 5. Circuit schematic of active diode [25].

The impedance of the piezoelectric transducer should be matched to an external load in order to deliver sufficient power. Therefore, an impedance matching circuit is required to be interfaced between the piezoelectric harvester and external load. The following equation expresses the input impedance of the piezoelectric harvester:

$$Z = \frac{1}{2\pi\omega \cdot C_p} , \quad (6)$$

where C_p is the electrical capacitance of the piezoelectric element, and ω is the resonant frequency of the harvester. The maximum power is extracted when the load impedance is the complex conjugate of the source impedance. Since the piezoelectric material has a high electrical capacitance, a matching circuit requires a bulky inductor to cancel its capacitive effect. Moreover, the value of the inductor should be variable depending on the resonant frequency, which is not feasible through the conventional passive inductor. Several solutions have been investigated in the literature to address this inductor emulation.

If the load impedance has only the resistance term, the optimum value should be $R_L = \sqrt{{R_s}^2 + {X_s}^2}$, in order to deliver maximum power. It can be seen that the optimum resistance is also dependent on the resonant frequency; however, making a variable resistive load is more practical than complex conjugate matching. For example, Wang et al. [26] propose a circuit based on maximum power point tracking (MPPT) method to achieve variable resistive load. A couple of switching techniques called as synchronized switch harvesting on Inductor (SSHI) [27], and synchronous electric charge extraction (SECE) [28], have been studied in the literature to accomplish complex conjugate matching. In the SSHI method, an inductor is placed across the output of harvester with a switch. At the start of each cycle, the switch closed for a short period to cancel the opposite charge of internal capacitance. In the SECE circuit, the switch closed at the peak voltage of each cycle to form an LC circuit. Then the charge of internal capacitor is completely transferred to the inductor to be used at the load part. Some of these power managing techniques will be used in our measurements in the following chapters.

Chapter 3
Deep-Learning-Based Optimization for a Low-Frequency Piezoelectric MEMS Vibration Energy Harvester

3.1. Introduction

In this study, we are motivated to design a new low-frequency MEMS piezoelectric vibration energy harvester with enhanced energy conversion efficiency. In this regard, a doubly clamped cantilever with a serpentine pattern associated with several proof masses is proposed to reduce the resonant frequency and to improve the overall efficiency. The proposed structure features multi-degrees of freedom, which can also offer the potential of operating at multiple mode shapes in order to expand the device bandwidth. To derive an optimal dimension considering our fabrication constraints, an optimization approach is required to accelerate the design process. The conventional optimization techniques including variant-mesh analysis and correlation matrix need massive human intervention to reach satisfactory results [29]. Thus, an automated design methodology with minimum

human effort based on genetic algorithm (GA) [30] has been adopted in this research to achieve the optimal performance for our proposed energy harvester.

While GA proves to be valuable for solving many hard problems, finding an effective fitness function to guide its evolution may be challenging due to either complex nonlinear modeling or high computation cost of application-specific simulation. For reduction of computation cost in optimizing problems whose design configuration space is highly complex or exact model is not readily available, e.g., large degrees of freedom associated, artificial intelligence (AI) has become very helpful for estimating system functionalities. An artificial neural network specifically with multiple layers between input and output, which is also known as deep neural network, is a powerful tool to model complex nonlinear relationship based on learning from the prepared data samples.

As an example of using deep learning for fault diagnosis of direct online induction motors, Zaman et al. [31] studied three graph-based semi-supervised learning methods. Based on the lab test data of a 0.25 HP induction motor under healthy, single- and multi-fault conditions, features for machine learning are extracted from the raw experimental stator current and vibration data with the discrete wavelet transform. This research concludes that the greedy-gradient max cut method is able to derive better classification results over the other alternatives. In another work, Zhao and Zhang [32] proposed an automated trial-and-error approach that combines reinforcement learning with deep learning for analog circuit sizing. Through the self-improvement learning way, the proposed method behaves like a designer, who learns from trials and derives experience,

evolving itself to finally discover the sizes that satisfy the performance specification based on simulation results.

In this chapter, we have proposed to train a deep neural network to model and predict the behavior of our newly devised MEMS harvester instead of using time-consuming FEM simulations or deriving complex analytical models for device geometry optimization. Eventually, our trained model was integrated with the genetic algorithm to optimize physical attributes of the harvester for the best performance. Our main contributions of this chapter are summarized as follows:

- We propose a serpentine-shaped piezoelectric MEMS energy harvester to lower operational frequency and enhance power efficiency in the first two vibration modes.
- To improve the performance of the proposed design, we have trained a deep artificial neural network with high accuracy. Our experimental results show that the trained model can predict device characteristics, such as resonant frequency and harvested voltage, with 90% accuracy.
- An automated design method combining GA and deep learning is developed to optimize the energy harvester in terms of operational frequency and harvested voltage.
- To demonstrate its manufacturability and validate its operation, we have prototyped the optimized harvester by using a micro-fabrication process. Our measurement

shows its superiority in terms of normalized power density and operational frequency compared to other studies.

The rest of the chapter is structured as follows. The design and modeling of the serpentine-shaped structure are described in Section 3.2. The deep artificial neural network is trained and tested as our model in Section 3.3. In Section 3.4, AI-based optimization is presented. The fabrication process is explained in Section 3.5. The simulation and measurement results are discussed in Section 3.6, followed by Section 3.7 as conclusion.

3.2. Design and Modeling

The structural diagram of the proposed low-frequency MEMS harvester is depicted in Fig. 6. This energy harvester is anchored on two sides, enclosing eight cantilever beams with deposition of thin piezoelectric material on their surface. The beams are linked together through seven proof masses, which make the device heavy enough for operating at low frequencies. The structure can be overall viewed as a doubly clamped serpentine cantilever with the capability of multi-degrees of freedom, including bending and torsional modes. The uniform distribution of masses over the device offers lower mechanical stiffness and larger deflection in comparison with regular piezoelectric cantilevers. All the beams are covered by a piezoelectric film, which are electrically unconnected from one another. Separate terminal pads are located on the unmovable substrate base to make an electrical connection with the corresponding electrodes on the piezoelectric layer. In this way, the whole surface of the device can become active areas for collecting electric charges.

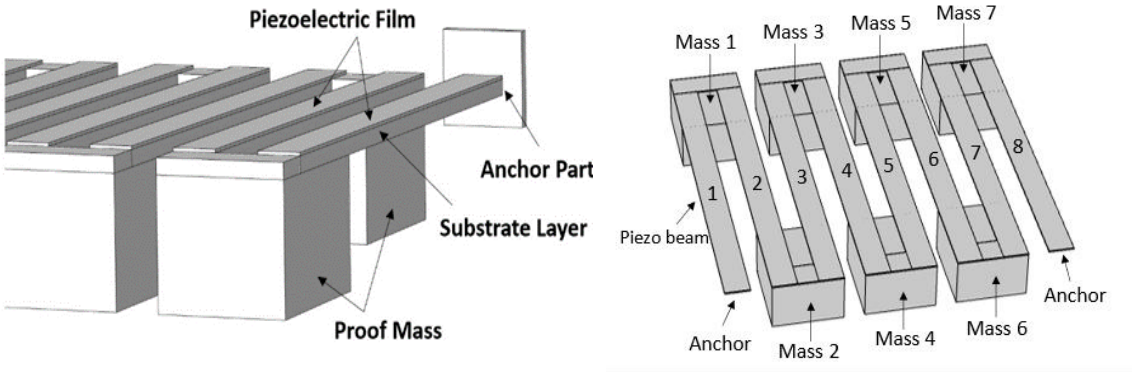

(a) (b)

Fig. 6. Schematic of the proposed low-resonant-frequency piezoelectric MEMS energy harvester: (a) side view, (b) top view

To investigate the functionality of the proposed energy harvester in different operational modes, the COMSOL Multiphysics software package (Version 5.4) was used for FEM simulations. For this purpose, we modeled the energy harvester in 3D space by using isotropic materials for the cantilever and piezoelectric layer. The Silicon (Si) material with the density of 2329 kg/m^3 and Young's modulus of 170 GPa was defined to form beams. A piezoelectric layer was made of Aluminium nitride (AIN) with the density of 2700 kg/m^3 and Young's modulus of 70 GPa. The simulation results for the first two modes are illustrated in Fig. 7. Obviously, involving a greater number of natural frequencies offers an opportunity to gain larger bandwidth. As the torsional effect does not heavily dominate the very first few modes of this structure, the rest of our optimization in this work strives to closely locate such frequencies (especially the first-mode resonant frequency) below or around 200 Hz to meet the requirement of low resonant-frequency operation.

According to Fig. 7, four masses on the opposite side of the two clamped parts (i.e., Mass1, Mass3, Mass5, Mass7) have maximum upward and downward vibration in the first mode, while the other three masses on the same side of the clamped parts (i.e., Mass2, Mass4, Mass6) vibrate with smaller amplitude in the identical phase but opposite to their counterparts. In the second mode, the anchor side masses (i.e., Mass2, Mass4, Mass6) maximally oscillate in the same phase, while the opposite side masses (i.e., Mass1, Mass3, Mass5, Mass7) have a smaller amount of oscillation with different phases. Such results reflect different directions and rates of curvature for each beam, which cause distinct charge polarity and power density in each mode. Thus, using a single connected piezoelectric layer for all the cantilevers may not be a good solution due to voltage cancellation. In such a situation, splitting the piezoelectric layer into discrete zones and applying proper circuitry are essential for improving the harvesting efficiency.

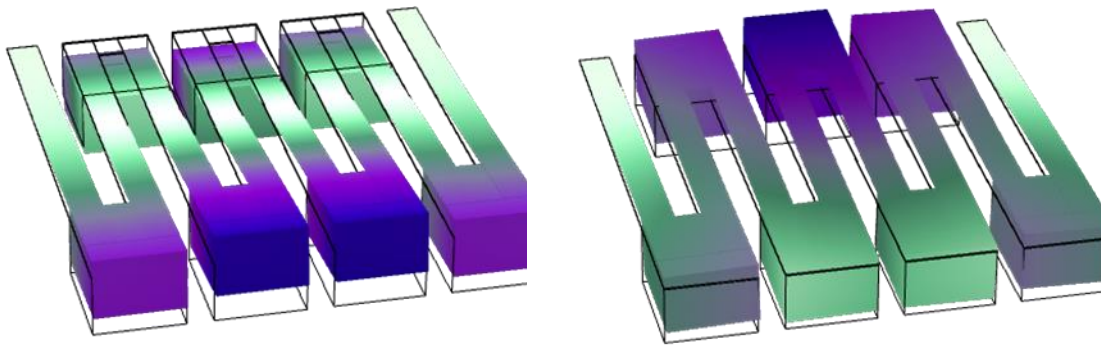

(a) (b)

Fig. 7. FEM simulations of the propsoed piezoelectric MEMS energy harvester: (a) the 1st mode shape at 125 Hz, and (b) the 2nd mode shape at 223 Hz.

The equivalent lumped parameter model of the proposed harvester is illustrated in Fig. 8 [33]. The equivalent stiffness and damping ratio of the *i*th beam is denoted by k_i and c_i respectively, and m_i refers to the equivalent *i*th mass. Since the size of the lateral beams (i.e., Beam 1 and Beam 8) are identical, the stiffness values of k_1 and k_8 can be considered equal and marked as k_l, and the stiffness values of the middle beams (i.e., $k_2, k_3, \dots, k_7$) can be assumed identical as k_m for the same reason. Thus, the mass and stiffness matrixes of the system can be written as:

$$[M] = \begin{bmatrix} m_1 & 0 & \dots & 0 \\ 0 & m_2 & \dots & 0 \\ \vdots & \vdots & \ddots & \vdots \\ 0 & 0 & \dots & m_7 \end{bmatrix}, \tag{7}$$

$$[K] = \begin{bmatrix} k_l + k_m & -k_m & 0 & 0 & 0 & 0 & 0 \\ -k_m & 2k_m & -k_m & 0 & 0 & 0 & 0 \\ 0 & -k_m & 2k_m & -k_m & 0 & 0 & 0 \\ 0 & 0 & -k_m & 2k_m & -k_m & 0 & 0 \\ 0 & 0 & 0 & -k_m & 2k_m & -k_m & 0 \\ 0 & 0 & 0 & 0 & -k_m & 2k_m & -k_m \\ 0 & 0 & 0 & 0 & 0 & -k_m & k_l + k_m \end{bmatrix}. \tag{8}$$

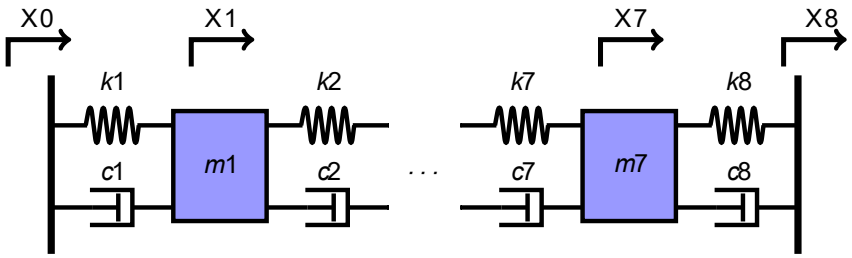

Fig. 8. The equivalent lumped parameter model of the proposed piezoelectric MEMS energy harvester.

With the mass and stiffness matrix, we can derive the eigenvalues and eigenvectors, which can help us obtain the natural frequencies and mode shapes of the system, respectively. By considering the Newton's 2nd law for the beams and Kirchhoff's loop law for the circuit, the electromechanically coupled equations of the piezoelectric energy harvester can be obtained [34] as follows,

$$m_i\ddot{X}_i + c_i\left(\dot{X}_i - \dot{X}_{i-1}\right) + k_i(X_i - X_{i-1}) + \alpha_i V_i = c_{i+1}\left(\dot{X}_{i+1} - \dot{X}_i\right) + k_{i+1}(X_{i+1} - X_i) + \alpha_{i+1}V_{i+1} \quad (9)$$

$$\alpha_i\left(\dot{X}_i - \dot{X}_{i-1}\right) - C_{pi}\dot{V}_i = V_i/R\,, \qquad i = 1, 2, \ldots, 7 \quad (10)$$

where X_i and $\ddot{X}_i$ denote the displacement and acceleration of the *i*th mass, respectively. It is worth mentioning that X_0 and X_8 refer to the substrate base displacement along the excitation direction. The constitutive voltage from the *i*th beam to the load resistance *R* can also be denoted by V_i, while the electromechanical coupling coefficient α_i and the electrical capacitance C_{pi} define the characteristics of piezoelectric elements that can be obtained from equations (1) and (2) presented in the previous chapter.

As an illustration, Fig. 9 depicts the maximum deflection of Mass 1 in the frequency domain obtained by FEM simulation and our proposed lumped parameter model above in the first mode. Although the proposed lumped model is able to qualitatively predict the dynamics of the devised harvester, it is still not able to precisely describe the exact characteristics of the mechanical system due to approximate modeling. Therefore, in the next section we will study how to utilize deep artificial neural network as an alternative to the analytical modeling in order to gain high accuracy without compromising computational efficiency for our specific optimization purpose.

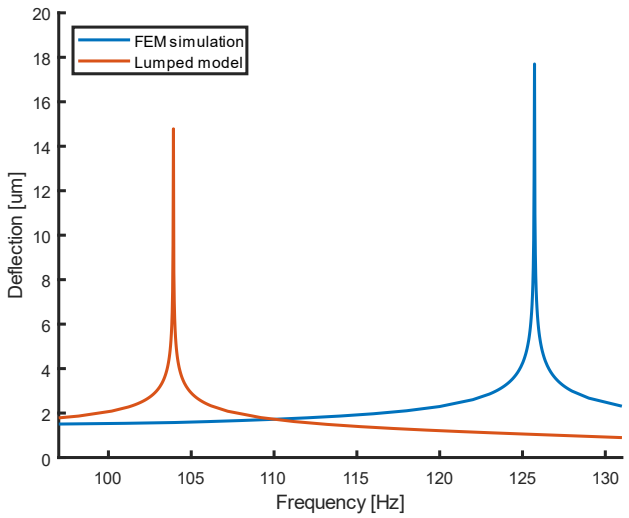

Fig. 9. Maximum deflection in the first mode obtained by the FEM simulation and the lumped parameter model.

3.3. Deep Learning Modeling

The artificial neural network (ANN) is a computing method which can learn from given samples to make decision or prediction. Their working principle is inspired by the

human brain to recognize complicated patterns between the inputs and outputs, like fault classification or machine translation [35]. The ANN is made up of smaller units known as neurons, which are connected through layers. Each neuron is composed of weights, which can map the inputs through an activation function to calculate the outputs. An artificial neural network with multiple hidden layers between the input and output layers is called a deep neural network (DNN). The learning rule of DNNs is based on a backpropagation algorithm to use gradient methods for reducing the loss function. In this algorithm, a prediction is made at each training step, and the output error is measured, then the algorithm goes back through each layer reversely to compute the error contribution of each neuron. Finally, the weights are updated in order to minimize the error at each step.

DNNs are able to map the inputs to outputs with a complex relationship. As a supervised machine learning algorithm, DNNs can be used for function approximation or nonlinear modeling by enough training with data samples generated by the actual system functions or simulations [36][37]. In this work, deep learning is used to replace highly accurate yet time-consuming FEM simulation or highly efficient yet coarse analytical modeling for our proposed serpentine structure to achieve the best trade-off between computation accuracy and efficiency in our harvester geometry optimization process. According to Fig. 10, four-dimension variables L_b, W_b, L_m, and W_m are considered as inputs to our DNN to obtain/output resonant frequency and harvested voltage. Obviously, these dimension variables are determining factors for the mass sizes and beam stiffness. Other design parameters like the thickness of beams or masses are supposed to be fixed values as per the fabrication process design rules or constraints.

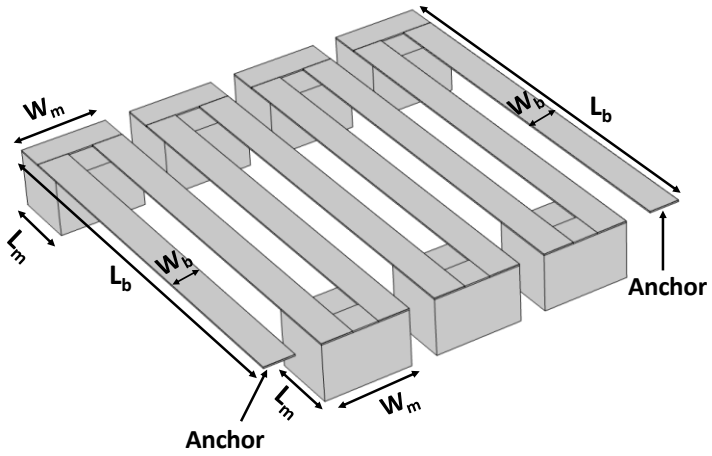

Fig. 10. Structure of the proposed piezoelectric MEMS energy harvester with its specified physical parameters.

Hyperparameter tuning is largely required to improve the generalization ability and computational time of DNNs, which are highly dependent on the fast and effective optimizer. A gradient-based optimization algorithm may easily be trapped into local minimums [38][39], which prevent training from convergence. Therefore, selecting an appropriate combination of activation functions and weight initialization methods is critical for efficient training. Finding a proper learning rate and batching size can also help gain faster training and prevent divergence. Number of hidden layers and number of neurons per layer are some other parameters that should be considered. Moreover, some regularization techniques such as the dropout method may become useful to avoid overfitting in DNNs [36].

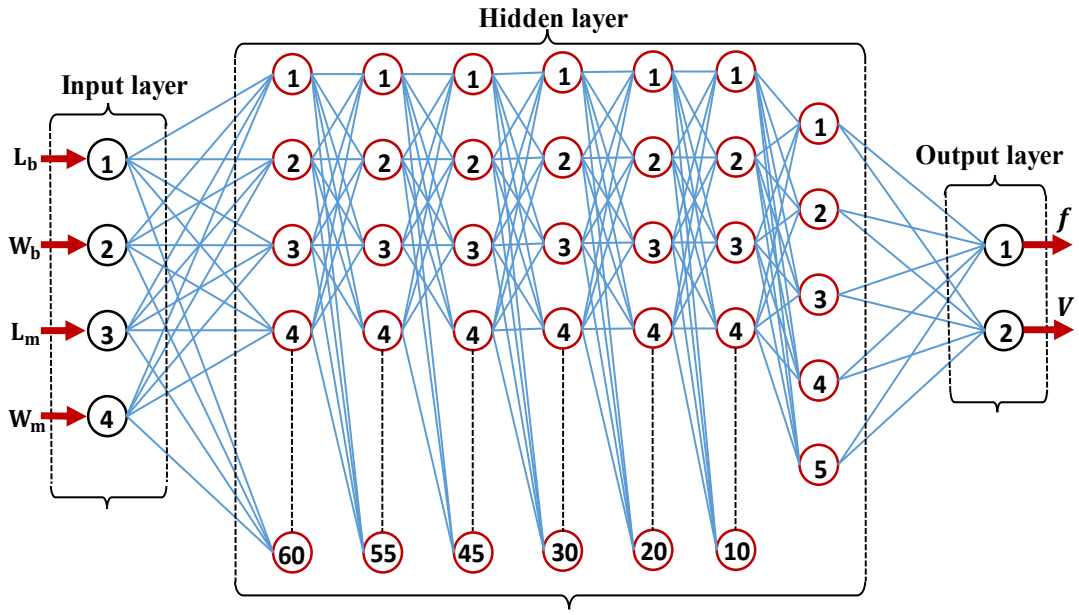

Fig. 11. Illustration of the utilized DNN for estimating the performance of the devised energy harvester.

The DNN shown in Fig. 11. is implemented for this study to improve the estimation accuracy and reduce the computation time in the optimization process. The four optimizable variables (i.e., L_b, W_b, L_m, and W_m) are fed into the network from the input layer. The network is comprised of seven hidden layers with 60, 55, 45, 30, 20, 10, and 5 neurons of sigmoid function at each layer, respectively. The output layer is formed by multiple neurons for obtaining the resonant frequency (f) and harvested voltage (V). A parametric sweep study over mentioned sizing variables is performed by COMSOL software to generate a dataset including 108 FEM simulation results for the training stage and 16 FEM data for testing. In the training stage, the Mean Square Error function and Gradient Descent with the learning rate of 0.01 are used as the loss function and the optimizer, respectively. The network is trained for 100 epochs with a batch size of 10. As

demonstrated in Fig. 12, the training and testing results indicate that the proposed DNN model can reach over 95 percent accuracy on the training data and 89 percent accuracy on the testing data. In the next section, the trained model is integrated with the evolutionary algorithm to optimize the dimension parameters of the proposed harvester.

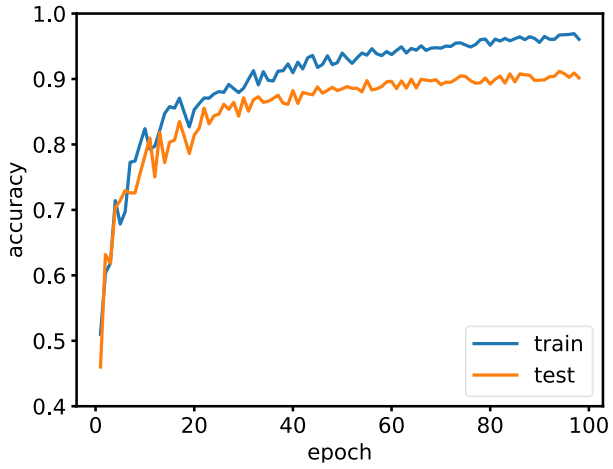

(a)

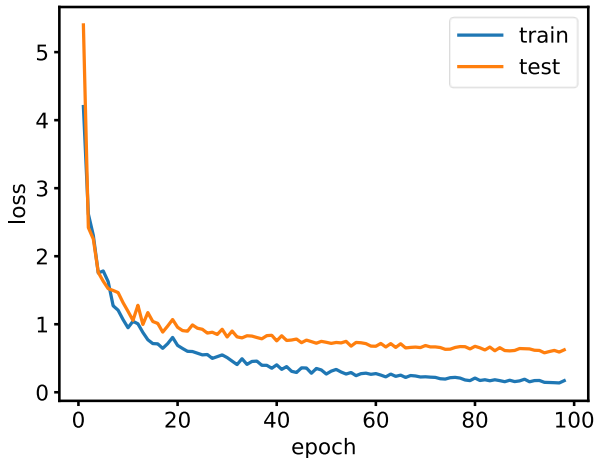

(b)

Fig. 12. (a) Training and testing accuracy over iteration. (b) Training and testing loss over iteration.

3.4. AI-Based Optimization

The GA is an evolutionary optimization method, which can be used for the optimization of complex problems by searching through constrained or unconstrained conditions [40]. The mechanism of GA is based on generating random values for multiple variables in a certain way to escape from local optima and approach the global optima [41]. The flowchart of the GA operation is depicted in Fig. 13. The algorithm starts by initializing a random population of *n* individuals. These variables are represented as fixed-length binary strings called chromosomes. Large population size can promote the GA's performance at the cost of more computational time.

After the initialization step, all individuals are evaluated by a fitness function and their superiority is ranked based on the fitness score that they received. The next step in GA is the selection phase, where two chromosomes with the highest fitness scores in the ranking are selected. In the crossover step, certain parts of strings are exchanged between the selected chromosomes. As a result of this combination, which is the most important step in the evolutionary algorithm, new pairs (called offspring) are produced. Eventually, in the mutation step, some bits of new offspring are changed from 1 to 0 or vice versa to ensure that the algorithm is not trapped into local optima.

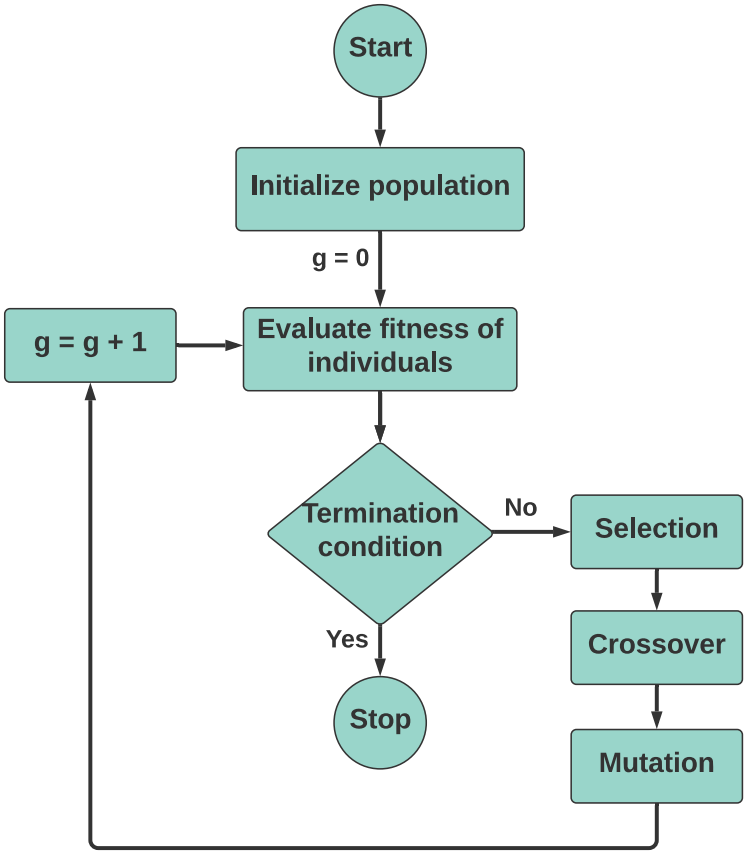

Fig. 13. Flowchart of the genetic algorithm.

After those three main operators of GA are performed, a new population is created by including new offspring. In the next cycle, the initial population is evolved to a new generation. If the termination criterion is met at this stage, the algorithm reports the best results and the procedure is stopped. If the loop does not terminate, the fitness evaluation is performed, and the algorithm is repeated for another round of evolutionary process. The parameter *g*, which increments at each iteration, indicates the total number of generations.

The genetic algorithm is normally used in two forms of problems (i.e., single-objective and multi-objective) depending on how many objectives are aimed at throughout the

evolution. For the multi-objective problems, which the real world challenges usually fall into, good trade-offs have to be made to achieve optimum objectives while still satisfying various constraints. In this study, our trained deep learning model described in Section 3.3 is used in the fitness function of the multi-objective GA to optimize frequency attribute and harvested voltage of the proposed energy harvester. Our AI-based GA optimization can be formulated as:

$$\begin{aligned} &\textit{Minimize}: \{f\} \\ &\textit{Maximize}: \{V\} \\ &\textit{Minimize: \{Silicon area\}} \\ &\textit{Subject to}: \text{design rules of the optimizable variables} \end{aligned} \tag{11}$$

where f is the natural frequency related objective(s), and V is the harvested voltage related objective(s). The algorithm strives to satisfy the defined objectives by optimizing the values of input parameters. In this regard, four dimension parameters, including beams length L_b, beams width W_b, mass length L_m, and mass width W_m, are considered as optimizable variables. The GA method then determines a set of optimal sizes for those physical dimensions of the harvester by using the trained DNN model to estimate f and V in (11). The upper and lower bounds of those optimizable variables are defined according to the fabrication technology design rules. For the same reason, the rest of the design properties listed in Table 1 are assumed to be constant.

We have implemented the proposed optimization process by using MATLAB genetic algorithm toolbox. A specific connection to the FEM simulations with COMSOL software

can be established through the Live-Link module to directly perform numerical analysis for the optimization toolbox. However, this has proved to be extremely inefficient since the computation time significantly increases due to large population size at each generation cycle. In contrast, the established DNN model can largely shrink such overhead incurred by the FEM simulations. Moreover, the training of the DNN model is just a one-time job, while the number of the training dataset is much smaller than that of the required FEM simulations within the plain GA-Live-Link optimization. The performance of the proposed AI-based optimization method in terms of reducing natural frequency and increasing voltage magnitude will further discussed in the following sections.

Table 1. Constant physical aspects of the serpentine-shaped energy harvester

Parameter	***Description***	***Size***
t_b	Thickness of the beams	10 μm
t_p	Thickness of the piezoelectric film	0.5 μm
h_m	Thickness of the proof masses	400 μm
Y_b	Young's modulus of the beams	70 GPa
ρ_b	Beam density	2700 Kg/m^3
Y_p	Young's modulus of piezoelectric material	50 GPa
ρ_p	Piezoelectric material density	7600 Kg/m^3
g_{31}	Piezoelectric material coefficient	-9.5e-V*m/N

3.5. Micro-Fabrication Process

To validate the performance of the proposed serpentine-shaped low-frequency piezoelectric MEMS vibration energy harvester, a prototype was fabricated by using the commercial PiezoMUMPs process from MEMSCAP Inc. This fabrication process consists of bulk and surface micromachining steps, as briefly described with the aid of Fig. 14 (a) – Fig. 14 (e). At the start of the process, a phosphosilicate glass (PSG) layer is deposited on the surface of 150 mm n-type silicon-on-insulator (SOI) wafer, which is then annealed up to 1050 °C for one hour in argon gas, as depicted in Fig. 14 (a). After that, the PSG layer is removed by using wet chemical etching, and then a 0.5 μm aluminum nitride (AlN) is deposited on the wafer as a piezoelectric film using the reactive sputtering technique. Afterwards, the wafer is coated with photoresist, and the piezoelectric film is lithographically patterned and wet etched as depicted in Fig. 14 (b). In the next step, a metal composite, consisting of 20 nm chrome and 1000 nm aluminum, is deposited on the piezoelectric layer as the top electrode through a liftoff process. After a lithographical patterning process, the deep reactive ion etch (DRIE) technique is used to etch down the silicon layer to the oxide layer, as shown in Fig. 14 (c).

On the front side of the wafer, the protection material is applied, as depicted in Fig. 14 (d). Then the RIE method is used to etch the substrate on the bottom side, as shown in Fig. 14 (e). Therefore, the silicon beams are formed due to the etched area of the substrate layer beneath the silicon layer, while the proof masses are released by the un-etched area of the substrate layer.

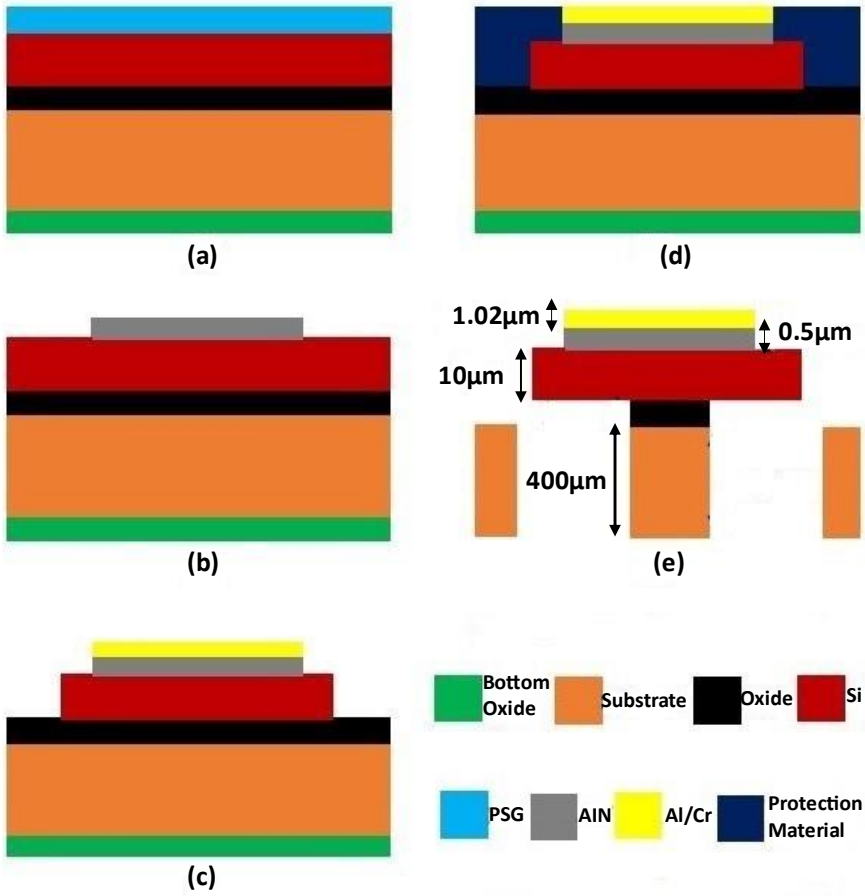

Fig. 14. Micro-fabrication process flow.

3.6. Experimental Results and Discussion

To improve the performance of the device, our proposed optimization method was performed with the population size of 20 and the generation number of 50 in our GA setup. Selecting proper values for these user-defined parameters is essential for reaching the best results. An un-optimized structure, named *Un-OPT*, is defined to demonstrate the effectiveness of the proposed AI-based optimization method for improving the frequency

attribute and the harvested voltage of the energy harvester. The optimizable variables (L_b, W_b, L_m, and W_m) were chosen to be the median values as per their allowed ranges in this un-optimized case. Additionally, for the comparison purpose, the lumped model and the COMSOL Live-Link module are also used as fitness evaluators for optimizing the dimensions in our experiments (called *LM-OPT* and *COM-OPT*, respectively).

Table 2. Performance evaluation of the un-optimized and optimized low-resonant frequency piezoelectric MEMS harvesters by using the lumped parameter model, FEM simulation, and DNN model.

Parameter	L_b [µm]	W_b[µm]	L_m [µm]	W_m [µm]	Freq. [Hz] (Lumped)	Freq. [Hz] (FEM)	Freq. [Hz] (DNN)	Voltage [mV] (Lumped)	Voltage [mV] (FEM)	Voltage [mV] (DNN)	Run Time [min.]
Range	[1550,3050]	[150,250]	[500,1000]	[600,615]	-	-	-	-	-	-	-
Un-OPT	2300	200	750	607	137	169	162	634	539	590	-
LM-OPT	2849	224	915	610	112	136	120	806	683	758	44
COM-OPT	2966	214	916	610	102	123	112	915	791	874	784
AI-OPT	2945	216	907	609	103	125	114	898	762	855	130

The obtained results for the un-optimized and optimized energy harvesting devices are summarized in Table 2. In this table, the allowed ranges for the optimizable parameters, which are specified by their design rule constraints, are listed in the second row. The computed natural frequencies by the lumped parameter model, FEM simulation, and DNN model for the un-optimized and optimized structures are listed in the 6th, 7th, and 8th columns. The calculated harvested voltages by the lumped parameter model, FEM

simulation, and DNN model under the excitation level of 0.1g at the resonant frequency, are presented in the 9^{th}, 10^{th}, and 11^{th} columns, respectively.

As listed in Table 2, the un-optimized harvester, named *Un-OPT*, can only operate at higher frequencies with less harvested voltage. The optimized device using the lumped model, named *LM-OPT*, has lower frequencies with higher voltage in comparison with the un-optimized one. However, one can observe that the accuracy of the lumped model in estimating the resonant frequency and harvested voltage is not high enough (only around 80 percent) in reference to the FEM simulations. Thus, a sound result may not be readily achieved by using this optimization method even with a large population size. The optimized device by using the COMSOL Live-Link module is also included in Table 2 as *COM-OPT*. Although this device can achieve better performance than that of *LM-OPT* due to the dedicated FEM-based optimization process, the computation time is too long (i.e., 784 minutes), which makes it hardly attainable.

Furthermore, the optimized device using the AI-based GA optimization method as discussed in Section 3.3 is labeled as *AI-OPT* in the Table. It can be observed that by performing this method with the population size of 20, the first natural frequency can be reduced by 25%, and the harvested voltage can be enhanced by 40%, in comparison to the un-optimized harvester. Its performance is also considerably better than that of the *LM-OPT* device. Although it takes 85 minutes more computational time for the FEM dataset generation (in the DNN model training process), this effort can be easily justified considering the fact that the DNN modeling method is more general than the specialism-

demanded analytical modeling. In addition, the DNN model training is just a one-time job for a certain mechanical structure. According to our experiments, the DNN can estimate both resonant frequency and harvested voltage with 90% accuracy in reference to the FEM simulations. Therefore, by utilizing the DNN as a performance evaluator in the fitness function, the computation time spent for FEM simulations can be significantly reduced. In this regard, the optimization runtime of *AI-OPT* can be shortened by 6 times compared to that of *COM-OPT*. Accordingly, a larger population size can be applied to enhance GA optimization effectiveness yet still maintaining sound algorithmic efficiency. Compared with the other alternatives, the optimized device *AI-OPT* is deemed as the best candidate considering the elegant trade-off between speedy optimization efficiency and superior MEMS energy harvesting performance thanks to its ultra-low operational frequency as well as high generated voltage.

To verify the performance of the proposed energy harvester experimentally, the optimized device *AI-OPT* was fabricated by using the described micro-machining process in Section 3.5. The experimental setup is shown in Fig. 10. In our measurement setting, a mechanical shaker (Type 4809 manufactured by Bruel & Kjær) was used to excite the prototyped energy harvester. The vibration frequency and magnitude were controlled by a function generator (Agilent 3250) and amplified by a high-power amplifier (manufactured by Bruel & Kjær). The shaker acceleration amplitude was monitored by an accelerometer (DXL 3350 manufactured by Analog Devices), which was attached to the shaker platform. Laser displacement sensors (LK-H022 manufactured by Keyence) were mounted on a support system on the top of the harvester to measure the deflection and the velocity of the

proof masses along the Z-axis over the time when the prototyped energy harvester was excited.

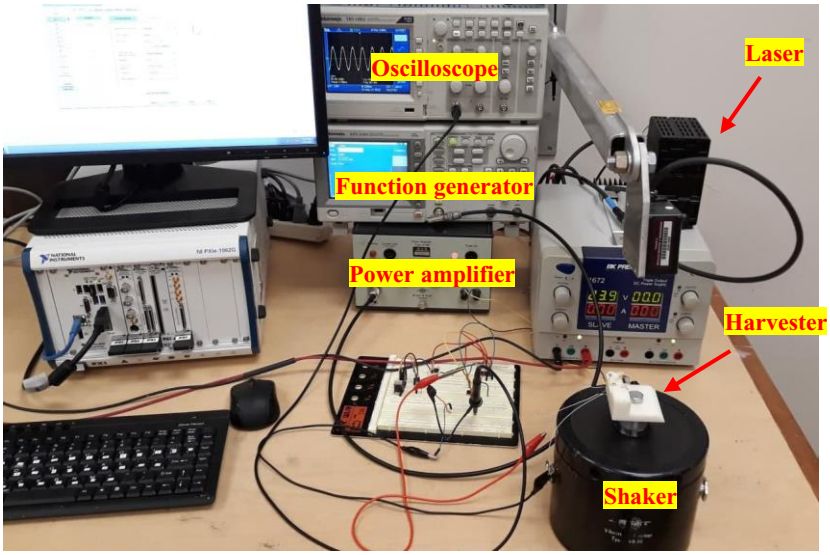

Fig. 15. Utilized experimental setup for measurement of the harvested voltages and operational resonant frequencies.

The frequency spectra of the prototyped structure derived by performing both FEM simulation and experimental measurements are depicted in Fig. 16. The velocity of each proof mass, i.e., Masses 1-7, is acquired by the laser displacement sensor while sweeping the operational frequency of the shaker in the range of 100 Hz - 250 Hz. Then the Fast Fourier Transforms (FFTs) of the recorded data (in time domain) is computed to obtain the frequency response. The two peak locations were observed at 121.7 Hz, and 216.6 Hz, representing the first and the second mode of the device, respectively. In Fig. 16 (a) and (c), one can observe that the Mass 3 and Mass 5 have maximum deflection in the first mode and have minimum deflection in the second mode. Similarly, Mass 1 and Mass 7 have larger velocity in the first mode, while their oscillation is less high in the second mode. In

Fig. 16 (b) and (d), it can be shown that Mass 4 maximally oscillates in the second mode compared to Mass 2 and Mass 6, while all of them experience considerable deflection in the first mode. For better comparison, Fig. 16 (e) and (f) also display both FEM simulated and measured velocity in the same plot for Mass 1 and Mass 2, respectively.

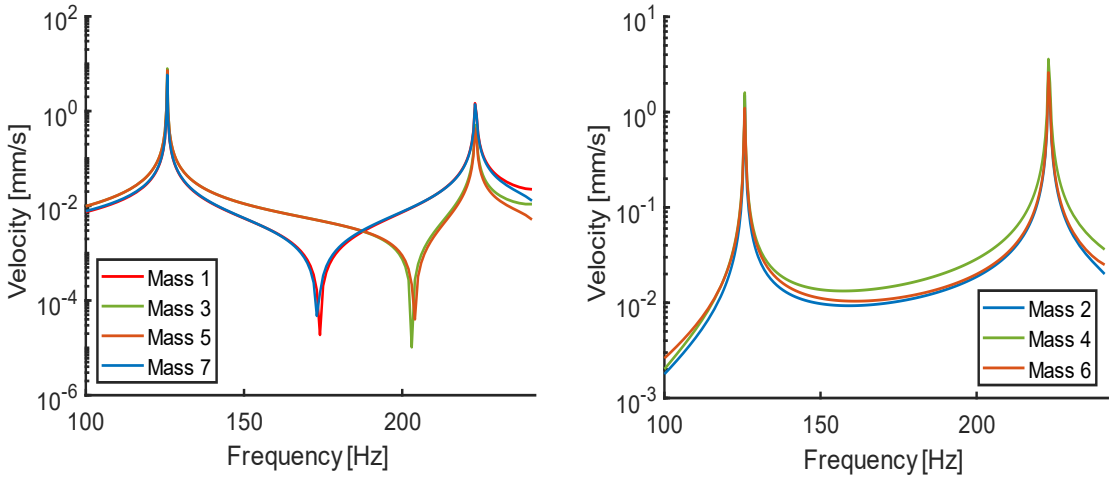

(a) (b)

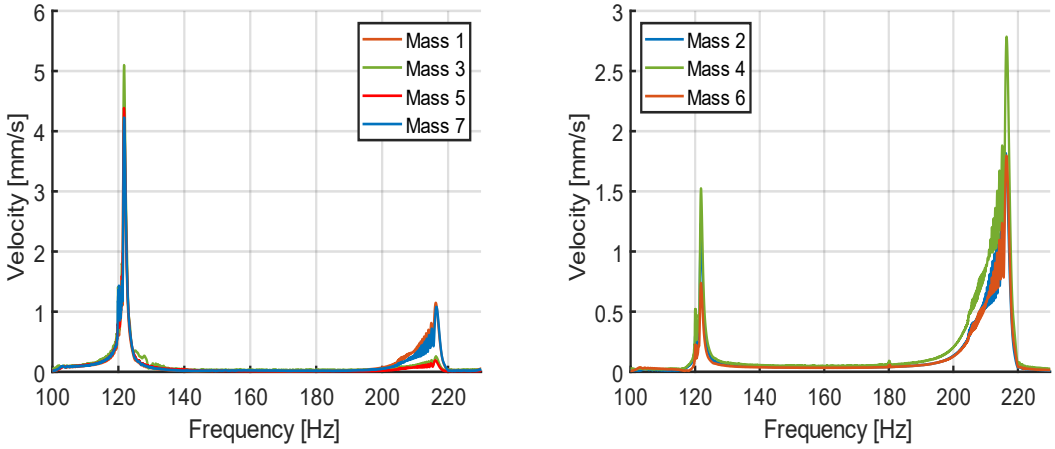

(c) (d)

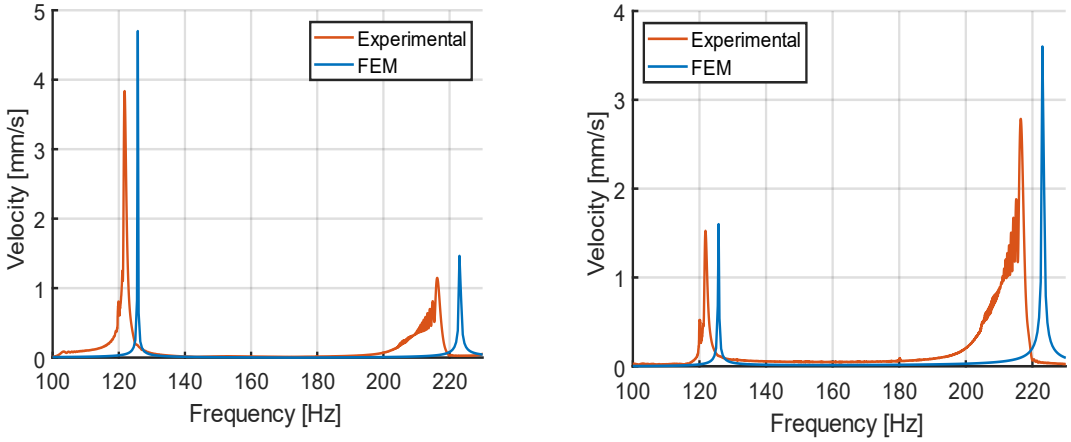

(e) (f)

Fig. 16. Frequency spectra obtained by performing (a)(b) FEM simulations, (c)(d) experimental measurements, (e) simulation and measurement for Mass 1, (f) simulation and measurement for Mass 4.

The stress distribution across the serpentine structure, which operates at the first and second mode resonant frequencies, is graphically displayed in Fig. 17. The Frequency Domain Study simulation is performed within COMSOL to obtain these numerical results. The structure was excited harmonically by applying the Body Load type acceleration of 0.1g at each mode shape. Our FEM simulations were conducted with a quality factor of 50, while the external force was applied in the Z-axis direction. According to Fig. 17 (a), when the energy harvester AI-OPT is oscillating in the first mode of vibration, the lateral beams are involved with a high level of stress, which gradually decreases when moving into the middle part beams. In Fig. 17 (b), it is shown that once the energy harvester AI-OPT is operating at the second resonant frequency, the second beam (i.e., Beam 2) and the second last beam (i.e., Beam 7) contribute the most to the generated stress, while a considerable amount of stress is also observed from the middle beams (i.e., Beams 3-6). Moreover, the

first and last beams (i.e., Beams 1 and 8) experience both tensile and compressive mechanical stress, which may result in electric charge cancellation in this mode.

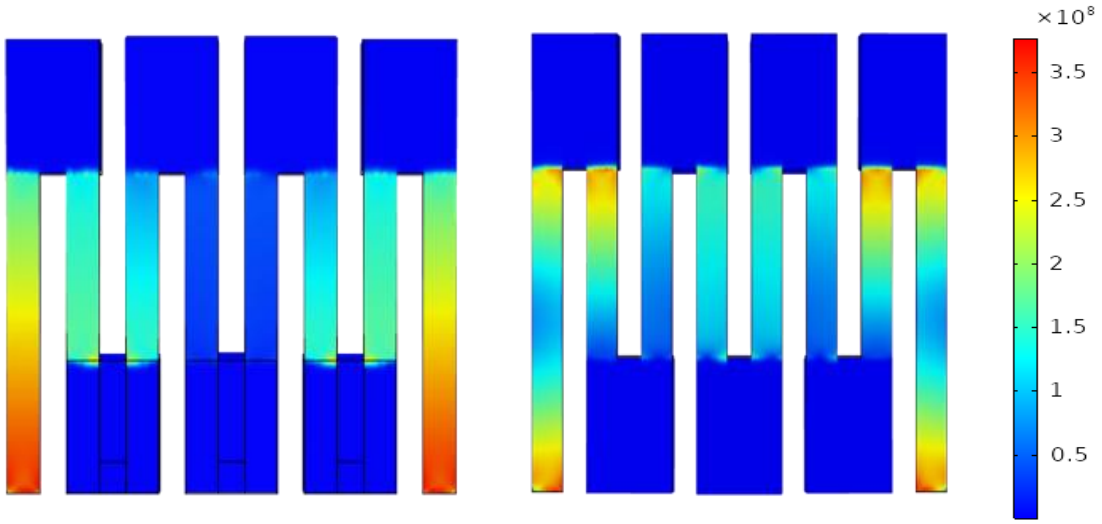

(a) (b)

Fig. 17. Von-Mises stress distribution on the cantilever surface of the proposed low-frequency harvester in the: (a) first and (b) second modes.

The longitudinal strains along the first and second beams are illustrated in Fig. 18. The strain analysis provides essential information that has to be considered for electrical connections. For example, the second beam has a negative strain in the first mode indicating its polarity opposite from the first beam, which means a reverse operation is needed during the electrical connection. In the second mode, the first beam has a positive strain on the anchor side, which gradually decreases to zero in the middle part and finally reaches a negative amount in the mass part. This nonlinear behavior also indicates that the bending direction is reversed along the beam. In such a situation, split electrodes are recommended in order to effectively capture electric charges.

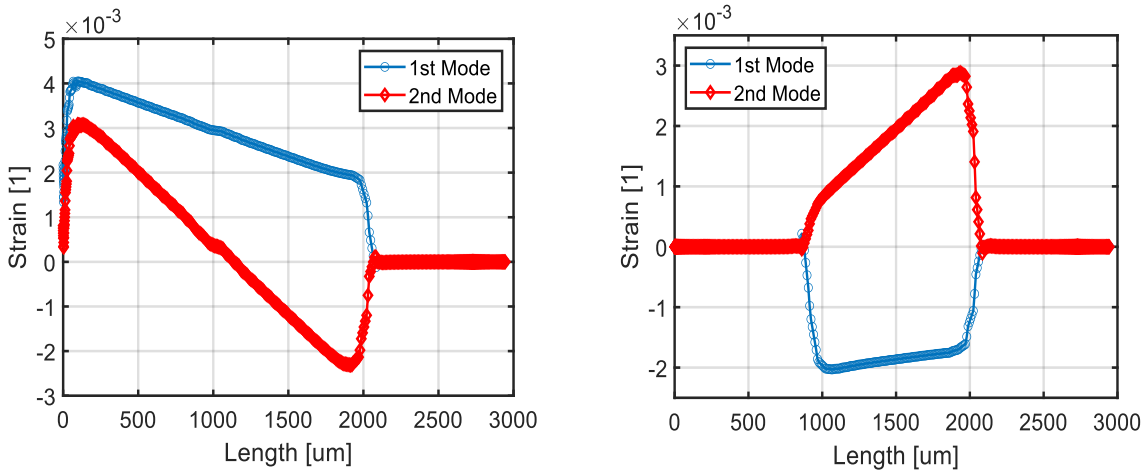

Fig. 18. Strain distribution magnitude in (a) Beam 1 (or 8), and (b) Beam 2 (or 7)

According to this analysis, in order to collect the electric charges more effectively, we divide the entire device into three separate regions, as shown in Fig. 19. In this regard, the first and third regions are considered as the most active part in the first mode of vibration, while the second region is considered as the dominant active part in the second mode. The electrodes of individual regions are connected in parallel so that their electric currents can be aggregated. The electrical connections are also managed based on polarity changes in order to avoid voltage cancellation.

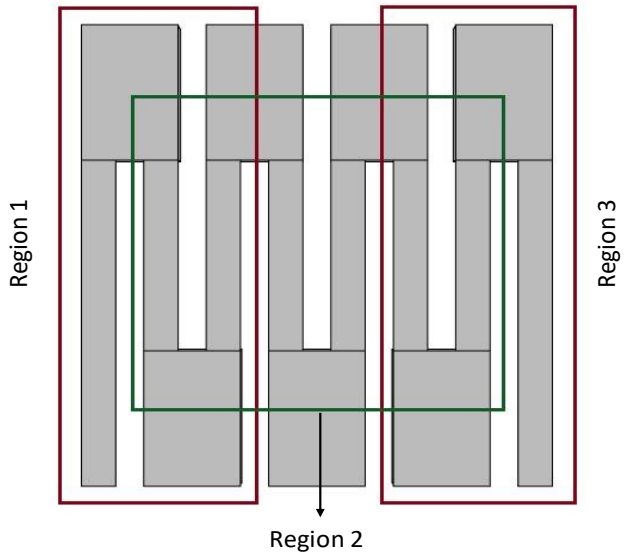

Fig. 19. Active regions at each mode shape.

The analysis of stress distribution confirms that at different mode shapes, almost the entire body of the device can harness the stress. In our proposed structure, unlike the conventional straight cantilever-based energy harvesters [42], the stress distribution keeps the active area of the device large enough, which can even collect energy from the regions far away from the clamped locations. In other words, all the segments of our proposed device participate in energy harvesting, which leads to higher power density for our energy harvester.

To further validate the capability of our prototyped energy harvester, the harvested voltage was measured by using a digital oscilloscope (DSA 7040 manufactured by Tektronix) through a high impedance probe. Fig. 20 illustrates the frequency response of the generated voltage in both vibration modes when the device is excited under the sinusoidal acceleration with the amplitude of 0.1g. It can be seen that the peak harvested

voltage, which is collected from Regions 1 and 3, can reach up to 643 mV in the first mode. Additionally, the peak collected voltage from Region 2 can be measured as 520 mV in the second vibration mode. Such results show that the measured voltage was a bit lower than the FEM simulation amount reported in Table 2, due to lower source impedance of the fabricated device [43].

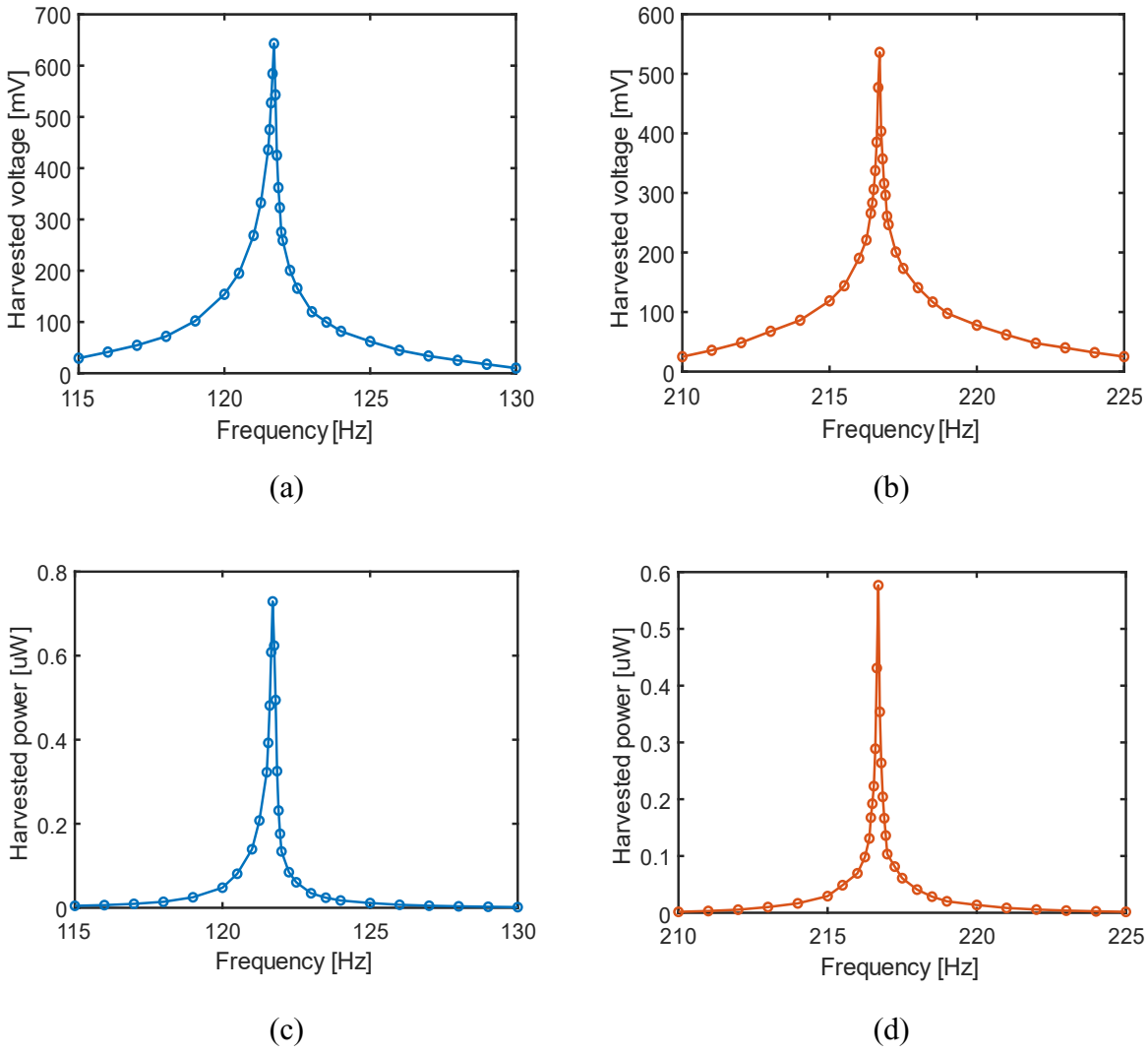

Fig. 20. Experimental measurement of (a) and (b): harvested voltage, and (c) and (d): harvested power, under sinusoidal acceleration of 0.1*g*.

To obtain the power density delivered to a load by our fabricated energy harvester, a proper impedance matching should be made by applying a resistive load equal to the source impedance of the prototype [44]. In this regard, the optimal load resistance of 72 KΩ and 67 KΩ, which are related to the first and second modes respectively, were measured experimentally. For the pure resistive loads, the average output power can be obtained by:

$$P_{avg} = \frac{V_{pk}^2}{2\,R_L} \quad (12)$$

where R_L is the optimal load resistance and V_{pk} denotes the peak voltage measured across the load. Fig. 20 shows that, when our prototyped MEMS device is excited by an input sinusoidal acceleration with the magnitude of 0.1g, it is able to generate 0.73 μW and 0.57 μW in the first and second modes, respectively.

To provide a comparison among the performance of different MEMS energy harvesters, the normalized power density (NPD), which is the amount of harvested power per occupied volume of the device times acceleration squared ($\mu W \cdot cm^{-3} \cdot m^{-2} \cdot s^4$), is widely used as a metric in the literature for determining the energy harvesting efficiency [45]. In this regard, a comparison of several attributes including NPD and operational frequency among our fabricated device and other energy harvesters reported in the literature is conducted as listed in Table 3. Comparison of the properties among the recently published piezoelectric MEMS vibration energy harvesters in the literature and our proposed harvester. Since the PZT is a highly efficient piezoelectric material, it can be seen that the energy harvesters

with PZT material normally have higher NPD in comparison with energy harvester with other piezoelectric materials. References [48] and [49] have low operational frequency below 100 Hz, but their NPD is pretty low. Although References [46], [50] and [54] have higher NPD than our proposed device, our device can resonate at a significantly lower frequency compared to them. In summary, our proposed energy harvester features both higher power density and lower operational frequency among the other AIN piezoelectric MEMS energy harvesters.

Table 3. Comparison of the properties among the recently published piezoelectric MEMS vibration energy harvesters in the literature and our proposed harvester.

Ref.	Material	Volume [mm^3]	Accel. [ms^{-2}]	Freq. [Hz]	Power [μW]	NPD [$\mu W .cm^{-3} \cdot m^{-2} s^4$]
[12]	PZT	0.11	2.45	68	23E-3	34.84
[47]	AIN	9.9E-2	49	2710	2.5	10.52
[48]	PZT	9.6	14.7	38.8	258	124.37
[46]	AIN	5	0.6	210	1.78	990
[50]	AIN	15	2	599	69	1150
[49]	AIN	18	1.96	84.5	0.13	1.97
[51]	PZT	4	5	126	5.3	53
[52]	AIN	1.63	10	857	0.18	1.1
[53]	PZT	17	1	143	1.74	102
[54]	PZT	0.02	39.2	1300	22	715
This work	AIN	1.5	1	121	0.73	486

3.7. Conclusion

In this chapter, we presented a low-frequency piezoelectric MEMS energy harvester that can operate in two bending modes. The proposed structure comprises a set of cantilevers with a serpentine pattern clamped at both ends. To provide the uniform mass distribution, seven proof masses are located at the junctions. A deep artificial neural network was trained to model the device performance in terms of physical aspects. It was shown that the trained model can estimate the device performance with an accuracy of 90%, which is a lot higher than the lumped parameter analytical model. Then this trained DNN model was used as a performance evaluator in the fitness function within a genetic algorithm in order to optimize the geometry of the device. The optimization result was validated through FEM-based simulations and prototype measurement. Our measurement results showed the proposed AI-based optimization method could reduce the device operating frequency to 121.7 Hz and improve the harvested power to 0.73 μW.

Chapter 4
Design and Optimization of a Bistable Energy Harvester Using Transfer Learning

4.1. Introduction

Capturing energy from the ambient parasitic vibrations is a perfect alternative to conventional batteries among the other renewable energy sources such as solar or thermal energy [3]. Unused vibration may be produced by ocean waves, wind flow, vehicles, or other environmental movements [56]. The kinetic energy of vibrations can be converted to electricity by using the techniques based on electrostatic, electromagnetic, triboelectric, and piezoelectricity. Many aspects of those techniques have been intensively studied in the literature for MEMS scale design. For tiny and portable applications, energy conversion based on piezoelectricity features higher power density and better compatibility with MEMS micromachining process in comparison to other techniques.

Energy harvesters with high operating frequency are not desirable considering the low-frequency characteristics of ambient vibrations. The operational frequency range (known as *bandwidth*) is another important characteristic that should be considered under an unpredictable or uncontrollable condition of ambient vibrations. The conventional piezoelectric energy harvesters typically use a single 1D cantilever with piezoelectric materials deposited on one side or both sides of the cantilever [57]. This simple structure basically has a high natural frequency, which needs to be matched with the low frequency and random vibration of external sources. The following methods have been explored in the literature to address the frequency tuning issues of vibration-based energy harvesters.

In general, reducing the cantilever stiffness can lower the resonant frequency, but it may reduce the effective mass and structure durability at the same time. Using large and connected proof masses is another way to lower the resonant frequency, but it may also affect the effective surface area in MEMS fabrication [58]. Several studies have proposed 2D cantilevers by using spiral, zigzag, and arc circular geometries to reduce the operational frequency [12][13] . In these designs, the effective surface area is increased, which helps to hold more power and lower resonant frequency. However, voltage cancellation may appear due to the emerging domination of torsional modes. Another solution to solving this problem is the frequency up-conversion technique by using impact or magnet-based methods [59][60]. For example, in the impact method [59], the stoppers are used to contact the beams and induce impulse response so that the low frequency oscillation of input from the ambient could be transferred to high frequency range suitable for the beams due to the

free vibration. The major issue with such settings is that the stoppers prevent this design from fitting into the MEMS scale.

A nonlinear method has been adopted by Xu and Kim [61] to both reduce the resonant frequency and expand the bandwidth. This design has a bistable buckled beam setup on the MEMS scale with doubly clamped boundary conditions and a large proof mass at the center of the beam. The analytical lumped model determines the softening and stiffening response of the system, while the experimental results exhibit higher power efficiency in softening response at lower frequencies than a mono-stable configuration. The nonlinear behavior of this design obviously makes the structure modeling more complicated in comparison with any linear forms. Besides that, the characteristics of the device become quite dependent on the level of input acceleration.

In this work, we are motivated to develop a new bistable MEMS piezoelectric energy harvester with the capability of operating at lower frequency range and larger bandwidth. For this purpose, an M-shape doubly clamped structure with a couple of proof masses is proposed to enhance the operational frequency features. The two-degree of freedom nature of the device also helps to gain larger bandwidth. In order to meet the best performance within the microfabrication constraints, a design methodology is required to attain the optimum geometry dimensions. Hence, a modified genetic algorithm (GA) is utilized in our work to accelerate the design process as it does not need a lot of human effort compared with other optimization methods [62].

Most of the stochastic approaches, including the genetic algorithm, require a fitness function for evaluating the performance during the optimization/evolution process. In the cases where the systems modeling is highly nonlinear and complex, the simulation tools can be used as a fitness function at the cost of high computation effort. Alternatively, the artificial intelligence, which is based on learning from data samples, can be used to overcome the computational overhead of simulations or the complexity of deriving the exact analytical model. For instance, by using artificial neural networks for image processing, the image can be directly inputted to the trained network for automatic pattern recognition without any complex feature edition/design. Zhang *et al*. [63] proposed a deep convolutional neural network (CNN) comprised of an encoder and a decoder for topology optimization. It is shown that their CNN model can solve the problem with less runtime despite minor performance drop compared to the conventional topology optimization approaches, e.g., SIMP (Solid Isotropic Material with Penalization) method.

As an example of using deep learning for reducing computation cost in topology optimization, Sasaki and Igarashi [64] trained a deep CNN to obtain torque properties of an interior permanent magnet (IPM) motor. In the learning phase, CNN is trained by the interior cross-sectional images of the motor in the red-green-blue (RGB) format. This trained model is further used as an approximate evaluation of most individuals in the stochastic optimization stage. The numerical finite element modeling (FEM) results indicate that the quality of optimization can reach a significantly high level if using the trained CNN model.

In the design of piezoelectric energy harvesters, analytical modeling is typically used along with FEM simulations to validate the design output. The device sizing optimization is to seek an optimal solution to the user-defined geometry features, such as beam length, beam width, mass size, and so on. Since the approximate lumped-parameter modeling for energy harvesters always shows a certain deviation from the exact analytical modeling, some correction factors may be needed to improve its accuracy. In this work, we propose a fast lumped-parameter model for our devised M-shaped harvester. We combine this lumped-parameter model with FEM simulation to form a deep neural network (DNN) through transfer learning, which can estimate the device behavior with higher accuracy. Then this trained DNN model is integrated with the genetic algorithm (GA) to optimize the geometry dimensions of the harvester and enhance its performance in terms of operating frequency and harvested voltage. The contributions of this chapter are highlighted as follows:

- We propose an M-shaped piezoelectric MEMS energy harvester with dual stable modes to operate in wider range at lower frequency;
- A deep artificial neural network is trained initially to emulate the lumped-parameter model of the harvester for estimating resonant frequencies and generated voltages;
- A pre-trained network is transferred to a new DNN model for another round of training with highly accurate FEM data samples to further reduce estimation error;
- An automated design method based on GA and deep learning is developed to optimize the geometry dimensions of the proposed energy harvester;

- The optimized harvester is prototyped by using a micro-fabrication process to demonstrate its manufacturability and validate its high performance.

The rest of this chapter is organized as follows. The design and modeling of the M-shaped harvester is described in Section 4.2. The AI-based optimization approach is discussed in Section 4.3. In Section 4.4, the fabrication process is presented. The simulation and measurement results are explained in Section 4.5. Section 4.6 concludes the paper.

4.2. Design and Modeling

The schematic of the proposed bistable MEMS energy harvester is depicted in Fig. 21. It is comprised of two main beams, which are clamped on both sides and connected to a large primary proof mass at the tip parts. A third auxiliary beam located parallel in the center along with a smaller tip proof mass on one end is also connected to the middle of the primary mass on the other end. The entire structure can be viewed as an M-shaped doubly anchored cantilever with dual bending mode. The surface of each beam is covered by a separate piezoelectric material, while the surface of each piezoelectric layer is covered by a metal layer electrically connected to its corresponding electrode terminal. The electrodes of the lateral beams are simply expanded to their terminal pads on the unmovable substrate, while the electrode of the middle beam is routed out to its associated pad by occupying a negligible area beside the adjacent beams.

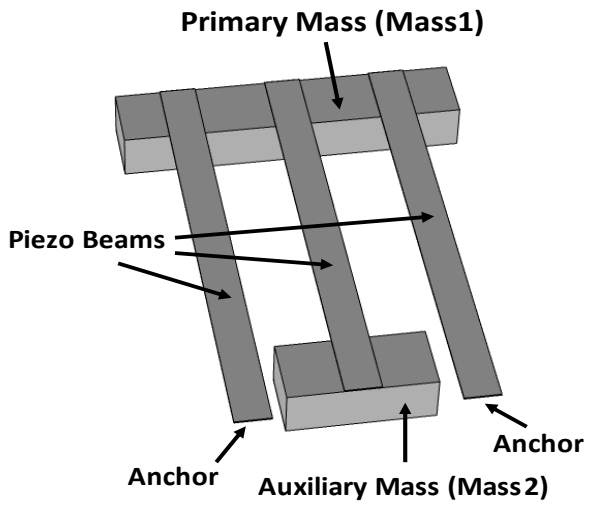

Fig. 21. Schematic of the proposed bistable piezoelectric MEMS energy harvester

The FEM simulation with the same setting as the one used in the previous chapter was performed in COMSOL Multiphysics to analyze the functionality of the proposed energy harvester. Fig. 22 displays the deflection and stress analysis of the device at both mode shapes. As shown in this figure, both proof masses have large deflection in the first vibration mode; however, most of the mechanical stress is imposed on the lateral beams while the middle beam has a low amount of stress. In the second mode, the primary mass has slight deflection whereas the auxiliary mass maximally oscillates. Furthermore, most of the stress is incurred on the middle beam, unlike the first vibration mode. According to this analysis, the electrical charges are supposed to be collected from the lateral beams in the first mode, and from the middle beam in the second mode, respectively. The rest of this work strives to locate these two mode shapes as close as possible to each other in the range of 100-200 Hz to reach both sufficient bandwidth and low operating frequencies at the same time.

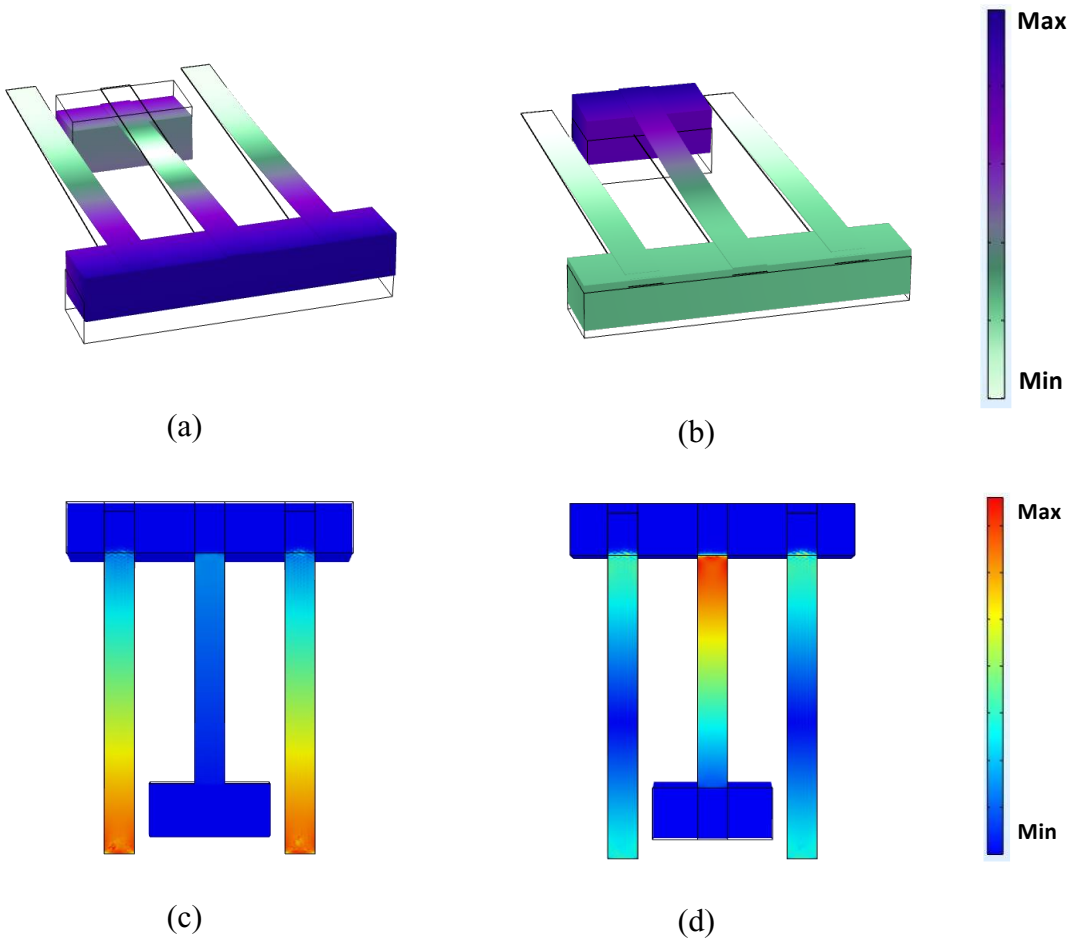

Fig. 22. FEM simulation results for mode shape ((a) and (b)) and stress analysis ((c) and (d)) for the first two modes.

Fig. 23 illustrates the equivalent lumped-parameter model of our proposed M-shaped harvester, where k_l denotes the equivalent stiffness of each lateral beam, k_m represents the equivalent stiffness of the middle beam, and m_1 and m_2 refer to the primary and auxiliary proof masses, respectively [65]. By considering the electromechanically coupled equations

of a piezoelectric energy harvester, the governing motion equation of the vibrating base is obtained [66]:

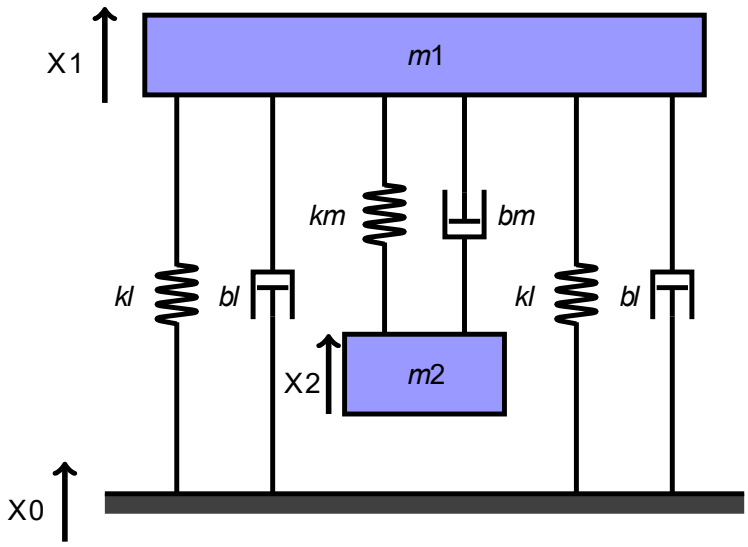

Fig. 23. The equivalent lumped-parameter model of the proposed M-shaped energy harvester.

$$m_1\ddot{X}_1 + 2b_l(\dot{X}_1 - \dot{X}_0) + 2k_l(X_1 - X_0) + \alpha_1 V_1 = k_m(X_2 - X_1) + b_m(\dot{X}_2 - \dot{X}_1) + \alpha_2 V_2 \quad (13)$$

$$m_2\ddot{X}_2 + k_m(X_2 - X_1) + \alpha_2 V_2 = 0 \quad (14)$$

$$\alpha_1(\dot{X}_1 - \dot{X}_0) - C_{p1}\dot{V}_1 = \frac{V_1}{R} \quad (15)$$

$$\alpha_2(\dot{X}_2 - \dot{X}_1) - C_{p2}\dot{V}_2 = \frac{V_2}{R} \quad (16)$$

where the displacement and acceleration of the primary mass are defined as X_1 and $\ddot{X}_1$, and those of the auxiliary mass as X_2 and $\ddot{X}_2$. The displacement of the substrate base along the excitation direction is denoted by X_0. The voltage of the load resistance R is denoted by

V, while the electromechanical coupling coefficient α and the electrical capacitance C_p defining the characteristics of the piezoelectric elements can be derived from the piezoelectric constitutive equation mentioned in chapter 2. According to (13)-(16) above, the mass and stiffness matrices can be expressed as:

$$[M] = \begin{bmatrix} m_1 & 0 \\ 0 & m_2 \end{bmatrix}, \quad (17)$$

$$[\mathrm{K}] = \begin{bmatrix} 2k_l + k_m & -k_m \\ -k_m & k_m \end{bmatrix} \quad (18)$$

By calculating the stiffness matrix, the special values and the special vectors, which relate to the natural frequencies and mode shapes of the system respectively, can be obtained. The proposed lumped model may need certain correction factors to describe the dynamics of the system with high accuracy. In the next section, this model is used along with FEM simulation data to train a deep artificial neural network through transfer learning to model the system more accurately for high-caliber optimization purpose.

4.3. Transfer-Learning-based Design Optimization

4.3.1. Transfer Learning Modeling

Deep neural network (DNN) is an artificial neural network with multiple hidden layers that can learn complex nonlinear relationships between multiple inputs and outputs under different operating conditions [67]. The DNN can be used as a function approximation after being trained with data samples created upon the actual system functionality [68]. The

learning rule is based on the gradient optimization algorithms to minimize the loss function. Thus, hyperparameter tuning is essential to achieve fast convergence to the global minimum [69]. Activation function, number of neurons and hidden layers, weight initialization method, and learning rate are some hyperparameters that should be selected properly. In this study, a DNN is utilized as an alternative to expensive FEM analysis or complex analytical modeling for estimating the natural frequencies and harvested voltages by taking five sizing variables L_b, L_m, W_{m1}, W_{m2}, and W_b, as shown in Fig. 24.

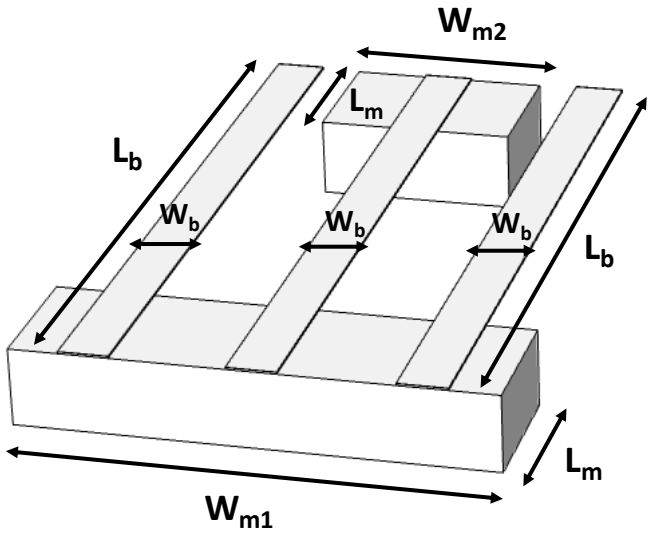

Fig. 24. Proposed M-shaped energy harvester with the specified physical parameters for geometry dimensions.

Training a deep neural network from scratch is not always the best idea. If we are tackling a supervised-learning task, but we do not have enough labeled training data, one solution is to find an auxiliary neural network with lots of labeled data, which can perform a similar task. Thus, we can reuse its lower layers for the main task of the original job. This

method is called *transfer learning*, making it possible to train a complex model faster but only with a few training data. In this regard, the original neural network does not have to learn all the low-level detailed features since it just reuses the feature detectors (i.e., in the lower layers) learned by the auxiliary neural network.

Kaur and Gandhi [70] proposed a deep convolutional neural network for brain magnetic resonance image (MRI) classification by using transfer learning. Several well-known pre-trained models, including Resnet50, GoogLeNet, Alexnet, Resnet101, VGG-16 were tested in this work to reach the best results. The validation shows that the transferred Alexnet model with an accuracy of more than 94% has the best performance compared to the other pre-trained models. In another work, Le *et al.* [71] proposed a framework with a combination of transfer learning and long short-term memory (LSTM) for energy consumption estimation in smart building research without much historical dataset. The results reveal that by transferring a pre-trained LSTM model to the proposed framework, the performance significantly increases with much less computational overhead in comparison with the other methods for energy consumption estimation.

In this study, the DNN shown in Fig. 25 is implemented for reducing FEM computational overhead during the optimization process. The network takes five optimizable parameters (i.e., L_b, L_m, W_{m1}, W_{m2}, and W_b) at the input layer and then goes through five hidden layers with 10, 20, 30, 20, and 10 sigmoid neurons at each layer, respectively. The last layer consists of four neurons that output both resonant frequencies and harvested voltages in the first two modes. Given that generating the whole dataset

using FEM simulations is too time-consuming, 768 data samples are created by the lumped-parameter model as described in the previous section. At the first step, the network is trained with 100 epochs using Adam optimizer with the learning rate of 0.1. After the first-step training, the first three layers of the trained DNN model are transferred to the new DNN, whose last two layers would be further trained.

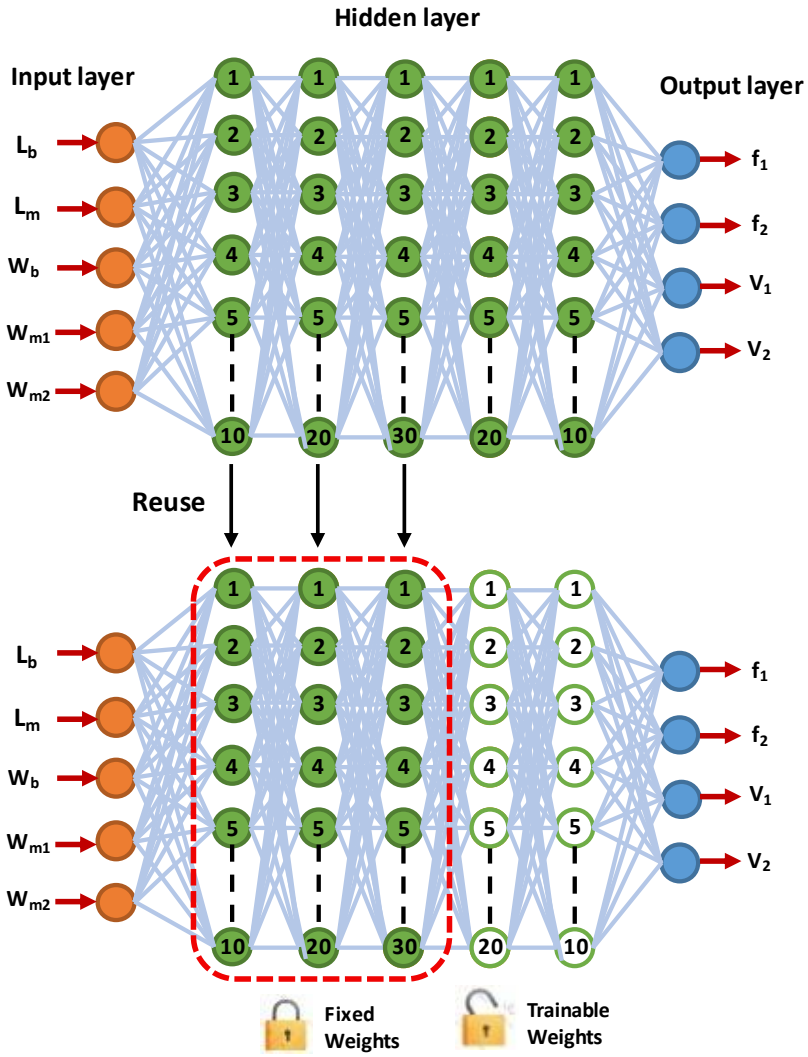

Fig. 25. Illustration of the proposed transfer learning method.

At the next step, 216 highly accurate FEM simulation results are created by using COMSOL parametric sweep study over the optimizable variables. Then the new DNN is trained for another round by using the newly available FEM simulation dataset. As the transferred layers have partially learned the behavior of the harvester, the weights of the first three layers remain frozen during the training while the weights of the last two layer stay trainable. Since the number of the parameters to be determined in the new DNN is significantly decreased, the last two layers would be much easier to be trained compared to the situation running from scratch.

For the testing phase, 32 more FEM simulation results are generated as the testing dataset. According to Fig. 26, the first DNN can only reach up to 86% accuracy on the test data, which is mainly due to the low accuracy of the lumped-parameter model dataset. However, the final DNN model can achieve over 94% accuracy thanks to the contribution from transfer learning. It is worth mentioning that before the second round of training, the new DNN model has the accuracy of 66% since it has partially trained. Fig. 26 (c) also exhibits the results for the DNN solely trained by the same number of the pure FEM simulation data without any pre-training. This model can only reach 90% accuracy on the test data after the same number of epochs. In order to increase the accuracy of this model, a larger dataset (i.e., much more than 216) is required, which means we need to additionally spend a significant amount of time on data collection (via FEM simulations) and more complex training process. In summary, we have leveraged the transfer learning technique to help improve modeling accuracy (around 4% higher) with the same dataset.

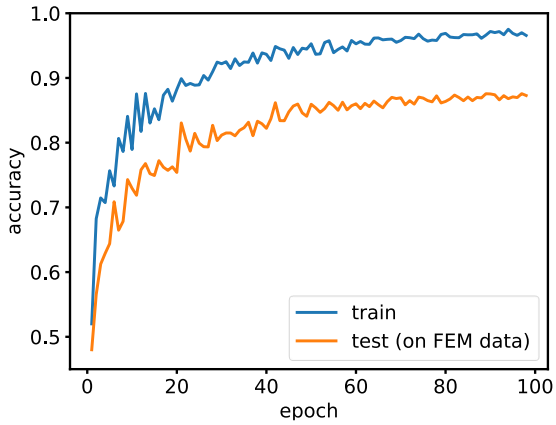

(a)

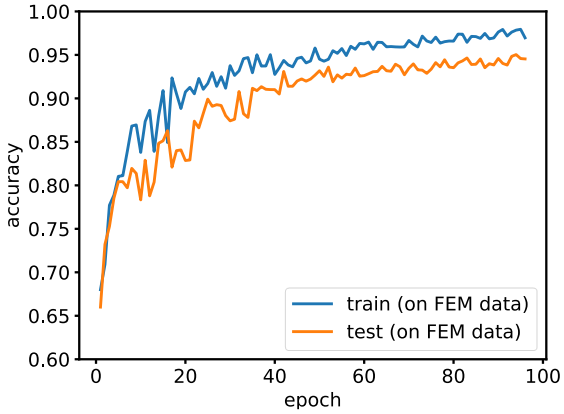

(b)

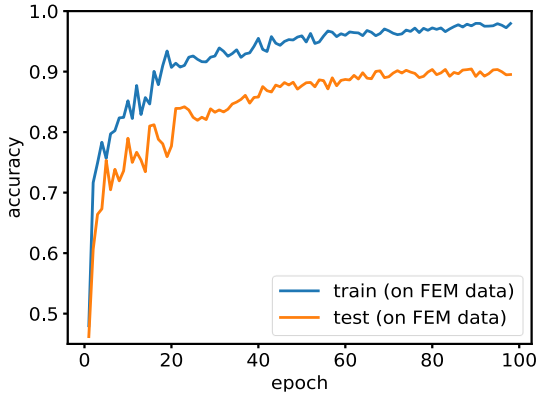

(c)

Fig. 26. Training and testing accuracy over iteration in (a) pre-trained DNN model, (b) final DNN model via transfer learning, (c) DNN model without pre-training (solely trained by FEM simulation data).

4.3.2. AI-Based Optimization

Genetic algorithm (GA) is a heuristic search-based evolutionary method that can be used for solving multi-objective optimization problems [72]. The GA requires a fitness function to evaluate the individuals at each generation cycle. In this work, the trained DNN model is utilized as a fitness function of GA to optimize the performance of the proposed M-shaped energy harvester. In this regard, the following objectives are defined to be optimized:

$$\begin{aligned} &\textit{Minimize: mean } (f_1, f_2) \\ &\textit{Minimize: } f_2 - f_1 \\ &\textit{Maximize: mean } (V_1, V_2) \\ &\textit{Minimize: } \{\textit{Silicon area}\} \\ &\textit{Subject to:} \text{ design rule constraints} \end{aligned} \tag{19}$$

where f_1 and f_2 are the first and second resonant frequencies, and V_1 and V_2 are the corresponding voltages at the first and second resonant frequencies. This algorithm strives to minimize the average operating frequency and their frequency range while maximizing the average of the harvested voltages. The beams length L_b, masses length L_m, mass1 width W_{m1}, mass2 width W_{m2}, and beams width W_b, are considered as the optimizable parameters in this optimization problem. The permitted bounds of these parameters and other constant properties are determined according to the manufacturing design rule constraints, as listed in Table 4.

Table 4. Sizes of the harvester physical aspects

Parameters	**Description**	**Size**
L_b	Length of the beam	2000 μm - 4000 μm
L_m	Length of the masses	500 μm - 1000 μm
W_{m1}	Width of the mass1	2000 μm - 3000 μm
W_{m2}	Width of the mass2	500 μm - 1500 um
W_b	Width of the beams	200 μm - 300 μm
t_b	Thickness of the beams	10 μm
t_p	Thickness of piezoelectric film	0.5 μm
h_m	Thickness of the proof masses	400 μm
Y_b	Young's modulus of the beams	70 Gpa
ρ_b	Beam density	2700 Kg/m^3
Y_p	Young's modulus of piezoelectric material	50 Gpa
ρ_p	Piezoelectric material density	7600 Kg/m^3
g_{31}	Piezoelectric material coefficient	-9.5e-3 V*m/N

Since the DNN model presented in Section 4.3.1 is integrated with the GA as a fitness function to optimize our proposed M-shaped energy harvester, we can finally derive the optimum geometry dimensions to reach the best performance while persevering the defined constraints. Although the COMSOL FEM simulation can also be used directly as a fitness evaluator through the Live-Link module, this solution seems too inefficient to be tolerated since the computational time may significantly increase due to the large number of evaluations. On the other hand, the DNN via transfer learning can largely release such computation overhead related to the FEM analysis so that a relatively smaller FEM simulation dataset can even perform a fine training.

4.4. Micro-Fabrication Process

The simplified micro-fabrication process flow, which was used to prototype the proposed piezoelectric MEMS device, is illustrated in Fig. 27. The process consists of five masks. First of all, the phosphosilicate glass (PSG) layer is deposited on the surface of Silicon-On-Insulator (SOI) wafer. Then, the PSG layer is removed by using wet chemical etching and the piezoelectric material, which is 0.5 μm of Aluminum Nitride (AlN), is deposited by using the reactive sputtering method. In the next step, a metal composite consisting of 20 nm chrome and 1000 nm is deposited as a top electrode through a liftoff process. Afterward, the silicon layer is lithographically patterned and etched down to the oxide layer by using the DRIE technique. Then the protection material is applied on the front side of the wafer, and the substrate layer on the bottom side is subsequently etched

into the oxide layer by using the RIE technique. Eventually the unimorph piezoelectric microcantilever containing the proof masses is released after completing these steps.

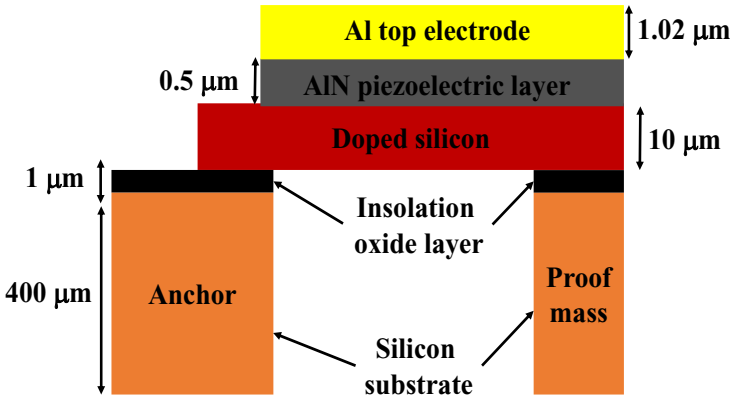

Fig. 27. The simplified micro-fabrication process to create piezoelectric MEMS cantilever with the integration of proof masses.

4.5. Experimental Results and Discussion

An un-optimized design (called NO-OPT) with median size in the allowed range for each optimizable parameter was chosen to serve as a reference design for comparison with the others in order to show the superiority of our proposed AI-based design and optimization methodology. The GA with generation number of 50 and population size of 20 was performed to optimize the device. The lumped-parameter model and the COMSOL software were also selected as fitness estimators for exhibiting fair comparison. The optimized devices using the analytical lumped-parameter model, COMSOL FEM simulation, and transfer-learning-based DNN are called ANA-OPT, FEM-OPT, and DNN-OPT, respectively. The design and performance results of those un-optimized and

optimized energy harvesters are listed in Table 5. The first and second operating frequencies, the frequency interval (i.e., bandwidth), and the mean harvested voltage under 0.2*g* input excitation reported by using FEM simulation for the various devices are presented in the 3rd, 4th, 5th, and 6th columns.

Table 5. Performance evaluation of the optimized and un-optimized proposed bi-stable piezoelectric MEMS harvester by using FEM simulations.

Parameter	**L_b, L_m, W_{m1}, W_{m2}, W_b [µm]**	**f_1 [Hz]**	**f_2 [Hz]**	**Frequency interval [Hz]**	**Mean harvested voltage [V]**	**Run time [min.]**
NO-OPT	2800, 700, 2400, 1000, 250	176	297	121	1.2	-
ANA-OPT	3486, 520, 2643, 1121, 268	132	188	56	1.6	40
FEM-OPT	3596, 549, 2722, 1082, 274	121	180	59	1.9	1140
DNN-OPT	3543, 539, 2630, 1108, 276	126.4	178.4	52	1.7	210

As shown in Table 5, the optimized design using the COMSOL live-link (FEM-OPT) can offer better performance than the other designs in terms of reducing the first natural frequency and harvested voltage. However, its computation time is extremely long (i.e., 1140 minutes) due to the large amount of FEM numerical simulations. Additionally, this module-based optimization usually experiences lots of unexpected glitches or even terminations during the execution process, which makes it hardly attainable in practice. On the other hand, the optimized design using the transfer-learning-based deep learning method (DNN-OPT) can deliver the best bandwidth among all the designs (note that

minimization of f_2 - f_1 is deemed as one of the objectives in (19) for GA optimization). Moreover, DNN-OPT requires significantly less runtime compared to FEM-OPT, which is mostly contributed by applying the transfer-learning-based DNN model as the fitness estimator in the GA optimization. It is worth mentioning that running a DNN model to generate output is much faster than invoking a FEM simulation. In addition, by using the transfer learning technique, we can improve the accuracy of the DNN model to 94% with reference to the accurate FEM analysis. Therefore, one can observe that the DNN-OPT device can reduce the first resonant frequency by 5.6 Hz and the bandwidth by 4 Hz in comparison with the ANA-OPT design. In summary, the optimized device DNN-OPT is considered as a qualified MEMS energy harvester for fabrication, thanks to its superior performance and robust reliability.

To experimentally validate the performance of our optimized design, the DNN-OPT energy harvester was fabricated through the PiezoMUMPS micro-machining process, which is described in the previous section. The scanning electron microscope (SEM) image of the prototyped device is shown in Fig. 28.

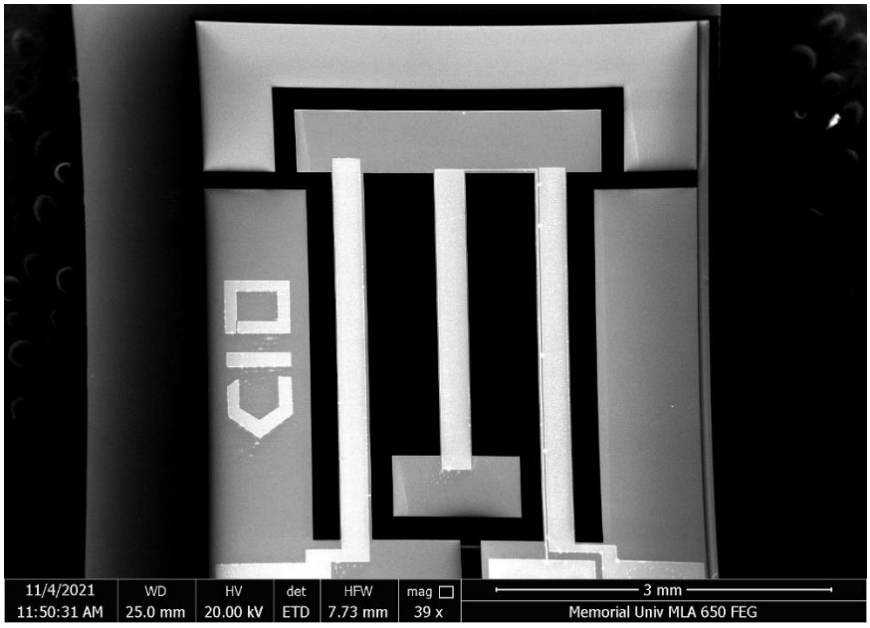

Fig. 28. SEM image of the fabricated M-shaped piezoelectric MEMS device.

Fig. 29 illustrates the frequency responses of the prototyped DNN-OPT device obtained by running FEM frequency analysis and experimental measurements. The mechanical shaker was set up to sweep the excitation frequency between 100 Hz and 200 Hz, and then the velocity of the primary and auxiliary masses was measured by the laser sensor. The frequency spectrum was obtained by computing the fast Fourier transforms (FFTs) of the acquired chirp signal. The first and second natural frequencies of the device were observed to be 123.8 Hz and 175.7 Hz, respectively. Since the prototyped device was tested in the air medium, the actual damping ratio may cause a deviation between the measured and simulated resonant frequencies. In addition, it can be observed from Fig. 29 that both masses have a considerable amount of deflection in the first mode. In the second mode, the auxiliary mass has the maximum deflection, while the primary mass slightly oscillates.

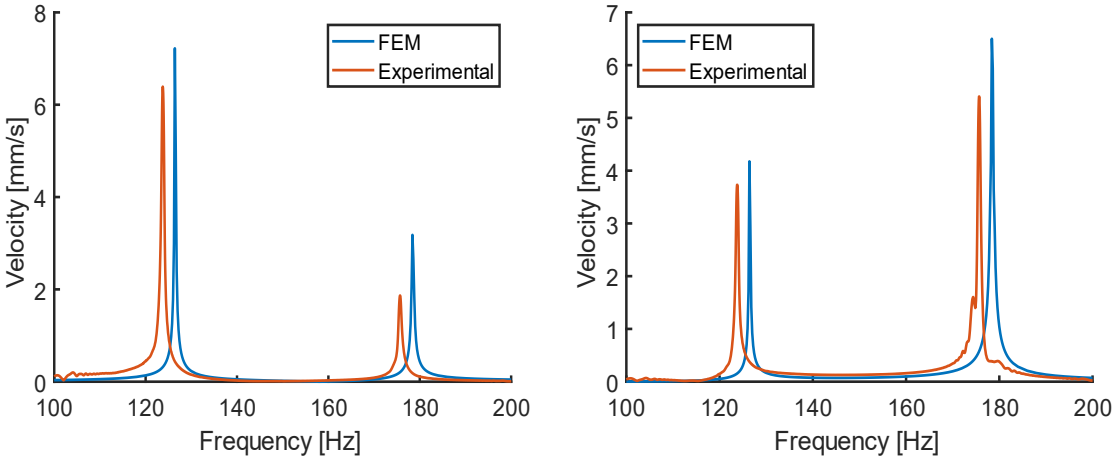

Fig. 29. Frequency response obtained by performing FEM simulations and experimental measurements on (a) Mass1, and (b) Mass2.

To verify the energy capturing capability of the prototyped device, the generated voltage was measured through a high impedance probe of a digital oscilloscope. The frequency spectra of the harvested voltages in both resonant modes, at 0.2g input excitation, were depicted inFig. 30. In the first mode, one can observe that the peak generated voltage coming from the lateral beams can be measured as high as 1.3 V. Moreover, the peak collected voltage from the middle beam can reach up to 1.6 V in the second mode. Since the measurements were performed in the air medium, the damping ratio may have caused certain voltage drop compared to the simulation results reported in Table 5.

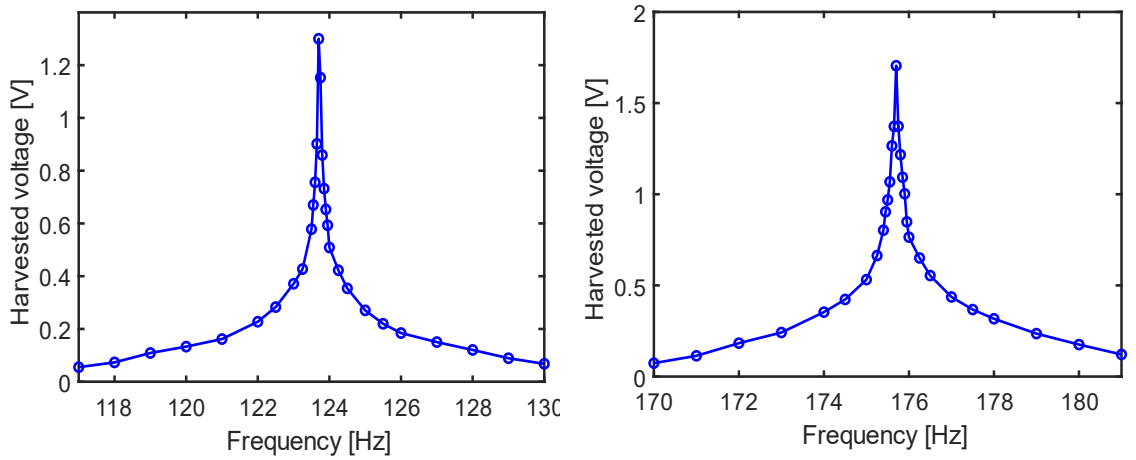

(a) (b)

Fig. 30. Experimental measurement results of the harvested voltages under sinusoidal acceleration of 0.2g, (a) in the first mode and (b) in the second mode.

In order to obtain the optimal load, the source impedance of the prototyped energy harvester was measured by Keysight Agilent E4990A impedance analyzer [73]. At the first and second resonant frequency, the source impedance was measured as 121 KΩ and 144 KΩ, respectively. A resistive load equivalent to the source impedance was applied to gain maximum power and impedance matching in each mode. According to equation $P_{avg} = (V_{peak})^2 / 2R_L$, it can be found that the peak harvested power is 2.83 μW in the first mode and 2.3 μW in the second mode at 0.2g sinusoidal input excitation.

In the literature, the normalized power density (NPD), which is the amount of harvested power per occupied volume of the device times acceleration squared ($\mu W \cdot cm^{-3} \cdot m^{-2} \cdot s^4$), is used to compare the performance of MEMS energy harvesters. As listed in Table 6, references [54][46][54] have slightly higher NDP than our proposed device; however, our device resonates at a much lower frequency compared to them (i.e., 1300 Hz and 210 Hz

versus our 123 Hz). References [61][12] have also superior operation frequencies, but their NDP is pretty low. Our prototyped energy harvester, featuring the first resonant frequency of 123 Hz, dual operational mode below 200 Hz, and NPD of 693 $\mu W \cdot cm^{-3} \cdot m^{-2} \cdot s^4$, offers a summit of superior efficiency and desirable spectrum compared to the other previously published studies. Moreover, considering only the first two operational modes, this harvester has 1.53 times higher NPD in comparison to our serpentine-shaped energy harvester proposed in the previous chapter. In the next chapter, a new structure with an ultra wideband operation will be discussed.

Table 6. Comparison of the properties among the recently published piezoelectric MEMS vibration energy harvesters in the literature versus our proposed harvester.

Ref.	Material	Volume [mm^3]	Accel. [ms^{-2}]	Freq. [Hz]	Power [μW]	NPD [$\mu W \cdot cm^{-3} \cdot m^{-2} \cdot s^4$]
[48]	PZT	9.6	14.7	38.8	258	124.37
[53]	PZT	17	1	143	1.74	102
[54]	PZT	0.02	39.2	1300	22	715
[46]	AIN	5	0.6	210	1.78	990
[47]	AIN	9.9E-2	49	2710	2.5	10.52
[20]	AIN	4.1	0.5	261	0.61	595.12
[12]	PZT	0.11	2.45	68	23E-3	34.84
[61]	PZT	22	2	20-80	0.08	9
This work	AIN	1.02	2	123	2.83	693

4.6. Conclusion

In this chapter, we presented a bistable MEMS energy harvester to provide a wider operation range at lower frequencies. The proposed design has an M-shaped cantilever with two proof masses and clamped at two sides. A deep artificial neural network is used along with analytical modeling to model the behavior of the harvester. Moreover, a transfer learning technique is employed to further improve the performance of the DNN modeling. In this regard, a fast lumped-parameter model is combined with FEM simulation to train a deep neural network that can estimate the system behavior with higher accuracy than the regular DNN. Finally, this trained model was integrated with a genetic algorithm to improve the performance of device and obtain optimum physical aspects. The experimental measurements confirm that the final optimized prototype has two bending modes at 123.8 Hz and 175.7 Hz with maximum harvested power of 2.83 μW, which reaches the submit among the recently published works.

Chapter 5

Design of Multimode Wideband Piezoelectric MEMS Energy Harvesters

5.1. Introduction

Energy harvesting from parasitic vibrations of ambient resources like human activity, wind flow, etc., has become a demanding solution to provide a sustainable power supply to low-power electronic devices [74]. The kinetic energy can be converted to electricity based on electromagnetic, electrostatic, triboelectric, and piezoelectric techniques [75]. In the MEMS scale applications, piezoelectric energy harvesting shows higher power capturing efficiency and more compatibility with the fabrications process [76]. Most piezoelectric MEMS harvesters are comprised of one end clamped single cantilever with deposited piezoelectric material on top of that. This simple structure has a quite narrow operating range that may not be practical for random natural vibrations. Thus, many studies have been conducted to address this issue.

In order to enlarge the bandwidth of energy harvesters, multiple cantilever beams (e.g. generator arrays) can be used to increase the degree of freedom and generate multiple mode shapes [77][22]. Other works studied frequency tuning and nonlinear techniques to increase the bandwidth. For instance, Wang and Tang [23] proposed magnetically coupled energy harvester with parasitic beam attached to the main body. The magnets can impose force to the beams and achieve two resonant peaks with highly nonlinear response. In these types of energy harvesters, the magnetic setup makes the fabrication incompatible with the MEMS micromachining process. In another work, Nabavi and Zhang [20] developed a tri-mode wideband energy harvester based on geometry with nonlinear behavior at the second mode shape. The amount of harvested power is limited in this device, although the large bandwidth could be achieved.

This chapter is organized as follows. A short discussion on wideband piezoelectric MEMS energy harvesters is introduced in this section. In the next section, the structure of our wideband energy harvester is proposed. In Section 5.3, the AI-based optimization methodology is discussed. Then the results and discussion are described in Section 5.4.

5.2. Multimode MEMS Piezoelectric Harvester

The structure of the proposed multimode energy harvester is presented in Fig. 31. This energy harvester has a symmetric flex-shaped configuration with a major middle cantilever beam anchored at one side. The other free side of the middle beam is split into two identical cantilevers increasing the degree of freedom of the system. Each of these cantilevers contains two more beams with proof masses to reduce operating frequency and improve

efficiency. Separate piezoelectric materials cover the beams with an electrode on top of them. These electrodes are routed out to corresponding terminal pads to make the electrical connections for charge collections.

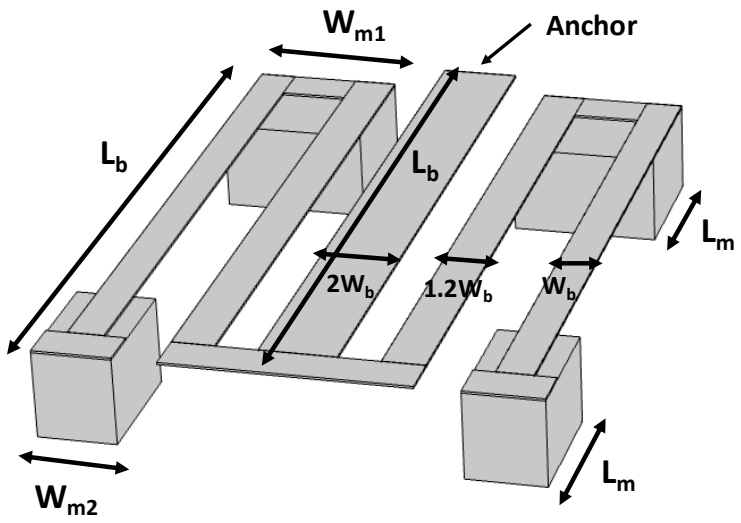

Fig. 31. Structural diagram of the proposed multimode MEMS energy harvester

5.3. AI-Based Optimization Methodology

In this study, the genetic algorithm, which is an evolutionary method for global optimization is used alongside deep artificial neural network as a fitness function to achieve optimal dimensions. The objectives of the optimization problem are set to minimize the operating frequencies and range. In this regard, the DNN shown in Fig. 32 was implemented as an alternative to complex nonlinear modeling or high computational cost simulation. This network is fed by five optimizable variables, i.e., L_b, L_m, W_{m1}, W_{m2}, *and*

W_b, at the input layer and outputs the first three natural frequencies. Five other hidden layers also consist of 20, 30, 40, 30, and 20 sigmoid neurons at each layer, respectively.

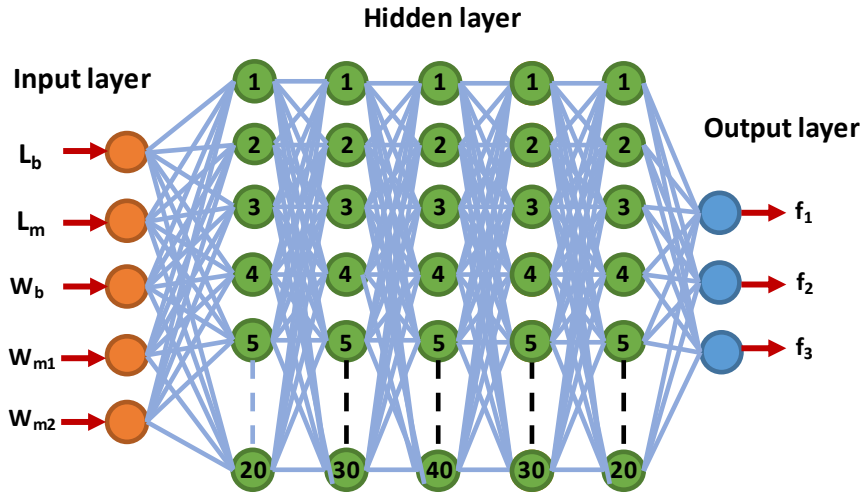

Fig. 32. Utilized DNN for estimating the resonant frequencies of the proposed multimode energy harvester

At the first stage, the network was trained with 245 FEM simulations data obtained by commercial COMSOL Multiphysics simulator with isotropic materials. The performance of the network was confirmed after reaching over 90% accuracy on the validation dataset. Afterward, this trained model was integrated with the genetic algorithm to obtain optimal aspects. At each cycle of GA, the individual samples are generated randomly to be evaluated by our implemented DNN in terms of operating frequencies. Eventually, the dimensions, which can provide lower resonant frequency and range, are selected by GA as the optimal solution.

5.4. Results and Discussion

The GA with the generation number of 50 and the population size of 20 was set up to perform the optimization process. An un-optimized design with median values of optimizable parameters is also defined to demonstrate the superiority of our AI-based method. The details of the optimized (OPT) and un-optimized (Un-OPT) harvester devices are shown in Table 1. The ranges for the dimension parameters, which are listed in the second row was determined by the fabrication design rule constraints. The primary three resonant frequencies and their mean intervals for both devices computed by FEM simulations are also listed in the 7^{th}, 8^{th}, 9^{th}, and 10^{th} column, respectively.

Table 7. Simulated resonant frequencies for the optimized and un-optimized design

Parameter	**L_b [µm]**	**L_m [µm]**	**W_b [µm]**	**W_{m1} [µm]**	**W_{m2} [µm]**	**f_1 [Hz]**	**f_2 [Hz]**	**f_3 [Hz]**	**Frequency Interval Sum [Hz]**
Range	(2000, 3000)	(400, 600)	(160, 180)	(400, 700)	(200, 400)	-	-	-	-
Un-OPT	2500	500	170	550	300	179	236	270	91
OPT	2773	589	164	654	357	132.7	174.6	194.4	61

According to the results summarized in Table 7, it could be observed that the proposed optimization method can reduce the first, second and third resonant mode by 25%, 26%,

28%, respectively. Moreover, the mean interval can also be reduced by 32% in comparison to un-optimized design. The frequency spectrum of the optimized device with the shape of our wideband harvester at each mode is illustrated in Fig. 33. The device exhibits a specific shape at each mode, which drives the device at multiple modes to attain the wideband feature. Furthermore, the harvested voltage of the optimized device was studied numerically under 0.25g input sinusoidal vibration. The generated peak voltage can be obtained as 1824 mV, 115 mV, and 1616 mV at the first, second, and third modes, respectively, which are also higher than the harvested voltage by the un-optimized design.

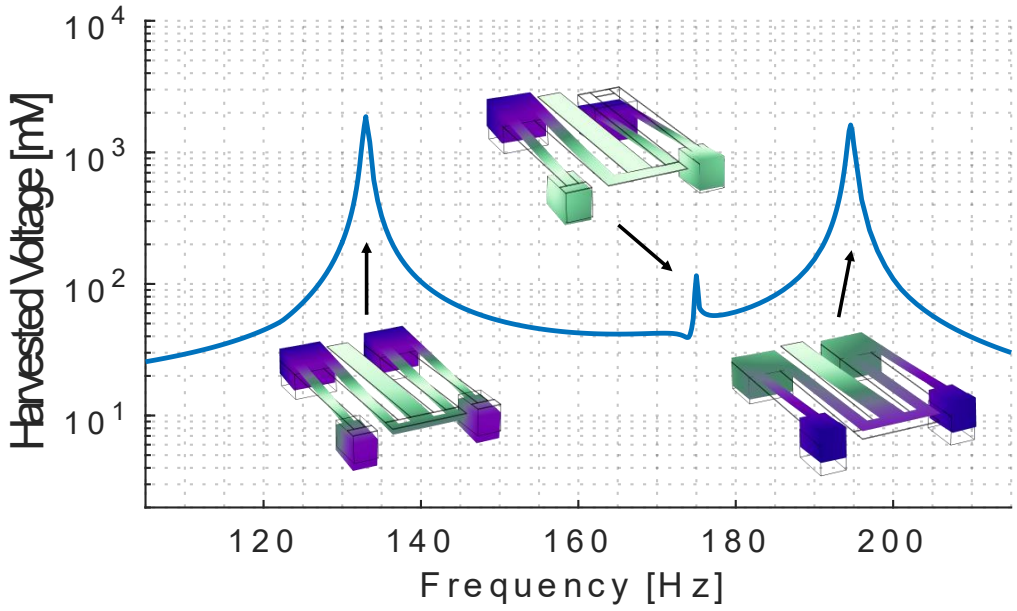

Fig. 33. Frequency spectra and mode shapes of the optimized wideband piezoelectric energy harvester.

In summary, the optimized energy harvester can have all the mode shapes coupled together at lower frequencies. Furthermore, by taking the advantage of DNN as a

performance estimator, we can reduce the computational time incurred by FEM analysis, so that larger number of individual variables can be evaluated during the optimization process.

Chapter 6 Conclusion and Future Work

In this thesis, we presented several newly devised piezoelectric MEMS energy harvesters with the capability of operating at low resonant frequencies (i.e., less than 200 Hz). The first structure has a symmetric serpentine structure with a doubly clamped configuration comprising several proof masses at the junctions. A deep artificial neural network was trained to model the device performance in terms of physical aspects. It was shown that the trained model can estimate the device performance with an accuracy of 90%, which is a lot higher than the lumped parameter analytical model. Then this trained DNN model was used as a performance evaluator in the fitness function within a genetic algorithm in order to optimize the geometry of the device. The optimization result was validated through FEM-based simulations and prototype measurement. Our measurement results showed the proposed AI-based optimization method could reduce the device operating frequency to 121.7 Hz and improve the harvested power to 0.73 μW.

In the second design, we presented an M-shaped energy harvester that can operate in two bending modes. In this work, a transfer learning technique is used to further improve

the performance of the DNN modeling. In this regard, a fast lump-mass model is combined with FEM simulation to form a deep neural network that can estimate the system behavior with higher accuracy than the regular DNN. The final optimized prototype also has larger bandwidth and 53% higher normalized power density compared to the previous serpentine-shaped design. Finally, in the last work, a flex-shaped multimode structure was proposed to satisfy the wideband feature. Once again, the AI-based optimization method is utilized to specifically lower the operating frequencies and enlarge the bandwidth in this design. The results indicated that the optimized device could locate three mode shapes sufficiently close to each other while vibrating at lower frequencies compared to the un-optimized device.

In all of the above-mentioned works, the deep-learning-based modeling helps to significantly reduce the computational overhead caused by the FEM simulations during the optimization process. As the future work, we intend to enhance our proposed AI-based optimization tool to deal with enlarging the operational bandwidth more efficiently. For this purpose, a more advanced function is required to be utilized as a performance estimator. Running intensive FEM simulation for either performance estimation or making more data samples may significantly increase the computational time. One feasible solution is to further improve the performance of our transfer learning method by using dropout regularization during the training phase or even using correction factors for the lumped-parameter model. The mechanical quality factor (Q) is another parameter that can considerably impact the operation of energy harvesters. The quality factor is defined as the resonant frequency over the 3 dB bandwidth. It is strongly dependent on the cantilever

geometry as well as the medium in which the device operates. The quality factor could also be added as an objective into our optimization methodology in future designs in order to further improve the performance of the energy harvesters.

References

[1] T. Ahmad and D. Zhang, “A critical review of comparative global historical energy consumption and future demand: The story told so far,” *Energy Reports*, vol. 6, pp. 1973–1991, 2020.

[2] C. Toro and N. Lior, “Analysis and comparison of solar-heat driven Stirling, Brayton and Rankine cycles for space power generation,” *Energy*, vol. 120, pp. 549–564, 2017.

[3] S. Khalid, I. Raouf, A. Khan, N. Kim and H. Kim, "A review of human-powered energy harvesting for smart electronics: recent progress and challenges", *International Journal of Precision Engineering and Manufacturing-Green Technology*, vol. 6, no. 4, pp. 821-851, 2019.

[4] S. Nabavi and L. Zhang, “Portable wind energy harvesters for low-power applications: a survey,” *Sensors*, 16(7): 1101, pp. 1-31, 2016.

[5] Q. Zhang and E. S. Kim, “Microfabricated electromagnetic energy harvesters with magnet and coil arrays suspended by silicon springs,” *IEEE Sens. J.*, vol. 16, no. 3, pp. 634–641, 2016.

[6] C. Liu, Foundations of MEMS. Upper Saddle River, *NJ: Prentice Hall*, 2012.

[7] A. Erturk and D. Inman, "A distributed parameter electromechanical model for cantilevered piezoelectric energy harvesters", *Journal of Vibration and Acoustics*, vol. 130, no. 4, 2008.

[8] H. J. Chilabi, H. Salleh, E. E. Supeni, A. As’Arry, K. A. M. Rezali, and A. B. Atrah, “Harvesting Energy from Planetary Gear Using Piezoelectric Material,” *Energies*, vol. 13, no. 1, p. 223, 2020.

[9] S. Nabavi and L. Zhang, “Curve-shaped anchor for durability and efficiency improvement of piezoelectric MEMS energy harvesters,” in *Proc. IEEE Sensors Conference*, pp. 1-4, 2018.

[10] L. Zhang, V. Masek, and N. Sanatdoost, “Structural optimization of Z-axis tuning-fork MEMS gyroscopes for enhancing reliability and resolution,” *Microsystem Technologies*, vol. 21, no. 6, pp. 1187-1201, 2015.

[11] S. Nabavi and L. Zhang, “T-shaped piezoelectric vibratory MEMS harvester with integration of highly efficient power management system,” *Journal of Physics: Conference Series (Power MEMS 2017)*, vol. 1052, no. 1, pp. 012102, 2018.

[12] H. Song, P. Kumar, et al., "Ultra-low resonant piezoelectric MEMS energy harvester with high power density," *Journal of Microelectromechanical Systems*, vol. 26, no. 6, pp. 1226-1234, Dec. 2017.

[13] D. Apo, M. Sanghadasa and S. Priya, "Vibration modeling of arc-based cantilevers for energy harvesting applications", *Energy Harvesting and Systems*, vol. 1, no. 1-2, 2014.

[14] N. Sharpes, A. Abdelkefi and S. Priya, "Two-dimensional concentrated-stress low-frequency piezoelectric vibration energy harvesters", *Applied Physics Letters*, vol. 107, no. 9, p. 093901, 2015.

[15] E. Dechant, F. Fedulov, D. Chashin, L. Fetisov, Y. Fetisov and M. Shamonin, "Low-frequency, broadband vibration energy harvester using coupled oscillators and frequency up-conversion by mechanical stoppers", *Smart Materials and Structures*, vol. 26, no. 6, p. 065021, 2017.

[16] I. Ahmad and F. Khan, "Multi-mode vibration based electromagnetic type micro power generator for structural health monitoring of bridges", *Sensors and Actuators A: Physical*, vol. 275, pp. 154-161, 2018.

[17] J. Iannacci, G. Sordo, E. Serra, and U. Schmid, “The MEMS four-leaf clover wideband vibration energy harvesting device: design concept and experimental verification,” *Microsyst. Technol.*, vol. 22, no. 7, pp. 1865–1881, 2016.

[18] J. Zhang and L. Qin, "A tunable frequency up-conversion wideband piezoelectric vibration energy harvester for low-frequency variable environment using a novel impact- and rope-driven hybrid mechanism", *Applied Energy*, vol. 240, pp. 26-34, 2019.

[19] S. Nabavi and L. Zhang, “Design and optimization of wideband multimode piezoelectric MEMS vibration energy harvesters,” *Multidisciplinary Digit. Publishing Inst. Proc.*, vol. 1, no. 4, pp. 586, 2017.

[20] S. Nabavi and L. Zhang, “Nonlinear multi-mode wideband piezoelectric MEMS vibration energy harvester,” *IEEE Sensors Journal*, vol. 19, no. 13, pp. 4837-4848, 2019

[21] J. Iannacci, E. Serra, G. Sordo, *et al.*, “MEMS-based multi-modal vibration energy harvesters for ultra-low power autonomous remote and distributed sensing,” *Microsyst. Technol.*, vol. 24, no. 12, pp. 5027–5036, 2018.

[22] X. Wei, X. Liu, C. Zheng, H. Zhao, Y. Zhong, Y.W.R. Amarasinghe, P. Wang, "A piezoelectric power generator based on axisymmetrically distributed PVDF array for two-dimension vibration energy harvesting and direction sensing", *Sustainable Energy Technologies and Assessments*, Volume 44, 2021,

[23] H. Wang and L. Tang, "Modeling and experiment of bistable two-degree-of-freedom energy harvester with magnetic coupling", *Mechanical Systems and Signal Processing*, vol. 86, pp. 29-39, 2017.

[24] S. S. Hashemi, M. Sawan and Y. Savaria, "A high-efficiency low-voltage CMOS rectifier for harvesting energy in implantable devices," in *IEEE Transactions on Biomedical Circuits and Systems*, vol. 6, no. 4, pp. 326-335, Aug. 2012.

[25] Y. Lu and W.-H. Ki, “Circuit Design of CMOS Rectifiers,” *Analog Circuits and Signal Processing CMOS Integrated Circuit Design for Wireless Power Transfer*, pp. 53–96, 2017.

[26] X. Wang et al., "A novel MPPT technique based on the envelope extraction implemented with passive components for piezoelectric energy harvesting," in *IEEE Transactions on Power Electronics*, vol. 36, no. 11, pp. 12685-12693, Nov. 2021.

[27] S. Du, Y. Jia, C. D. Do and A. A. Seshia, "An efficient SSHI interface with increased input range for piezoelectric energy harvesting under variable conditions," in *IEEE Journal of Solid-State Circuits*, vol. 51, no. 11, pp. 2729-2742, Nov. 2016.

[28] M. Meng, D. Wang, B. D. Truong, S. Trolier-McKinstry, S. Roundy and M. Kiani, "A multi-beam shared-inductor reconfigurable voltage/SECE mode piezoelectric energy harvesting interface circuit," in *IEEE Transactions on Biomedical Circuits and Systems*, vol. 13, no. 6, pp. 1277-1287, Dec. 2019.

[29] G. Sordo, E. Serra, U. Schmid, and J. Iannacci, “Optimization method for designing multimodal piezoelectric MEMS energy harvesters,” *Microsyst. Technol.*, vol. 22, no. 7, pp. 1811–1820, Jul. 2016.

[30] L. Zhang, R. Raut, Y. Jiang, U. Kleine, and Y. Kim, “Macro-cell placement for analog physical designs using a hybrid genetic algorithm with simulated annealing,” *Integrated Computer-Aided Engineering*, vol. 12, no. 4, pp. 379-396, Sep. 2005.

[31] S. Zaman, X. Liang, and L. Zhang, “Induction motor fault diagnosis using graph-based semi-supervised learning,” in *Proc. IEEE Canadian Conference on Electrical and Computer Engineering*, pp. 1-5, 2020.

[32] Z. Zhao and L. Zhang, “Deep reinforcement learning for analog circuit sizing,” in *Proc. IEEE International Symposium on Circuits and Systems*, pp. 1-5, 2020.

[33] S. Baishya, D. Borthakur, R. Kashyap and A. Chatterjee, "A high precision lumped parameter model for piezoelectric energy harvesters," *IEEE Sensors Journal*, vol. 17, no. 24, pp. 8350-8355, 15 Dec.15, 2017.

[34] A. Erturk and D. Inman, "On mechanical modeling of cantilevered piezoelectric vibration energy harvesters", *Journal of Intelligent Material Systems and Structures*, vol. 19, no. 11, pp. 1311-1325, 2008.

[35] S. Zaman, X. Liang, and L. Zhang, “Greedy-gradient max cut-based fault diagnosis for direct online induction motors,” *IEEE Access*, vol. 8, pp. 177851-177862, 2020.

[36] M. Ahmadi and L. Zhang, “Analog layout placement for FinFET technology using reinforcement learning,” in *Proc. IEEE International Symposium on Circuits and Systems*, pp. 1-5, 2021.

[37] S. Nabavi and L. Zhang, “Design and optimization of a low-resonant-frequency piezoelectric MEMS energy harvester based on artificial intelligence,” in *Proc. of 32nd Eurosensors Conf.*, vol. 2, no. 13, p. 930, 2018.

[38] T. Liao and L. Zhang, “Parasitic-aware GP-based many-objective sizing methodology for analog and RF integrated circuits,” in *Proc. 22nd Asia South Pacific Design Automat. Conf. (ASP-DAC)*, pp. 475-480, 2017.

[39] Z. Liu and L. Zhang, “Performance-constrained template-driven retargeting for analog and RF layouts,” in *Proc. ACM Great Lakes Symposium on VLSI*, pp. 429-434, 2010.

[40] S. Nabavi and L. Zhang, "Design and optimization of piezoelectric MEMS vibration energy harvesters based on genetic algorithm," *IEEE Sensors Journal*, vol. 17, no. 22, pp. 7372-7382, 2017.

[41] L. Zhang and U. Kleine, "A genetic approach to analog module placement with simulated annealing", in *Proc. IEEE International Symposium on Circuits and Systems*, pp. 345-348, May 2002.

[42] S. Nabavi and L. Zhang, “Frequency tuning and efficiency improvement of piezoelectric MEMS vibration energy harvesters,” *IEEE Journal of Microelectromechanical Systems*, vol. 28, no. 1, pp. 77 – 87, 2019.

[43] S. Nabavi and L. Zhang, “T-shaped piezoelectric structure for high-performance MEMS vibration energy harvesting,” *IEEE Journal of Microelectromechanical Systems*, vol. 28, no. 6, pp. 1100-1112, 2019.

[44] S. Nabavi and L. Zhang, “Design and Optimization of MEMS Piezoelectric Energy Harvesters for Improved Efficiency,” in *Proc. IEEE Sensors Conference*, pp. 1-3, 2017.

[45] A. Brenes, A. Morel, et al., "Large-bandwidth piezoelectric energy harvesting with frequency-tuning synchronized electric charge extraction", *Sensors and Actuators A: Physical*, vol. 302, p. 111759, 2020.

[46] Y. Jia and A. A. Seshia, “Power optimization by mass tuning for MEMS piezoelectric cantilever vibration energy harvesting,” *J. Microelectromechanical Syst.*, vol. 25, no. 1, pp. 108–117, 2016.

[47] A. Alameh, M. Gratuze, M. Elsayed, and F. Nabki, “Effects of proof mass geometry on piezoelectric vibration energy harvesters,” *Sensors*, vol. 18, no. 5, p. 1584, 2018

[48] X. Dong, Y. Zhiran, K. Lingchao, T. Yingwei, L. Jingquan, and Y. Bin, “Design, fabrication, and characterization of bimorph micromachined harvester with asymmetrical PZT films,” *J. Microelectromechanical Syst.*, vol. 28, no. 4, p. 700, 2019.

[49] M. Rezaeisaray, M. El Gowini, D. Sameoto, D. Raboud, and W. Moussa, “Low frequency piezoelectric energy harvesting at multi vibration mode shapes,” *Sens. Actuators A, Phys.*, vol. 228, pp. 104–111, Jun. 2015.

[50] R. Elfrink, M Renaud, et al., “Vacuum-packaged piezoelectric vibration energy harvesters: Damping contributions and autonomy for a wireless sensor system,” *J. Micromech. Microeng.*, vol. 20, no. 10, p. 104001, 2010.

[51] K. Morimoto, I. Kanno, K. Wasa and H. Kotera, "High-efficiency piezoelectric energy harvesters of c-axis-oriented epitaxial PZT films transferred onto stainless steel cantilevers", *Sensors and Actuators A: Physical*, vol. 163, no. 1, pp. 428-432, 2010.

[52] T. H. Hirasawa, Y. T.-T. Yen, P. K. Wright, A. P. Pisano, and L. Lin, “Design and fabrication of piezoelectric aluminum nitride corrugated beam energy harvester,” in *Proc. Power MEMS*, pp. 211–214, 2010,

[53] E. Suwa, Y. Tsujiura, F. Kurokawa, H. Hida and I. Kanno, "Fabrication of high-efficiency piezoelectric energy harvesters of epitaxial Pb(Zr,Ti)O3 thin films by laser lift-off", *Energy Harvesting and Systems*, vol. 3, no. 1, 2016.

[54] A. Hajati and S. Kim, "Ultra-wide bandwidth piezoelectric energy harvesting", *Applied Physics Letters*, vol. 99, no. 8, p. 083105, 2011.

[55] M. Gholikhani, H. Roshani, S. Dessouky, and A. Papagiannakis, “A critical review of roadway energy harvesting technologies,” *Applied Energy*, vol. 261, p. 114388, 2020.

[56] C. Covaci and A. Gontean, "Piezoelectric energy harvesting solutions: A review", *Sensors*, vol. 20, no. 12, p. 3512, 2020.

[57] N. Sezer and M. Koç, "A comprehensive review on the state-of-the-art of piezoelectric energy harvesting", *Nano Energy*, vol. 80, p. 105567, 2021.

[58] L. Wang, D. Lu, et al., "A piezoelectric cantilever with novel large mass for harvesting energy from low frequency vibrations", *AIP Advances*, vol. 8, no. 11, p. 115205, 2018.

[59] G. Hu, L. Tang, R. Das, and P. Marzocca, “A two-degree-of-freedom piezoelectric energy harvester with stoppers for achieving enhanced performance,” *International Journal of Mechanical Sciences*, vol. 149, pp. 500–507, 2018.

[60] P. Deepak and B. George, "Piezoelectric energy harvesting from a magnetically coupled vibrational source," in *IEEE Sensors Journal*, vol. 21, no. 3, pp. 3831-3838, 1 Feb.1, 2021.

[61] R. Xu, H. Akay, and S.-G. Kim, “Buckled MEMS beams for energy harvesting from low frequency vibrations,” *Research*, vol. 2019, pp. 1–14, 2019.

[62] S. Sunithamani, P. Lakshmi, and E. Eba Flora, “PZT length optimization of MEMS piezoelectric energy harvester with a non-traditional cross section: Simulation study,” *Microsyst. Technol.*, vol. 20, no. 12, pp. 2165–2171, Dec. 2014.

[63] Y. Zhang, B. Peng, X. Zhou, C. Xiang, and D. Wang, “A deep convolutional neural network for topology optimization with strong generalization ability,” *arXiv.org*, 31-Mar-2020.

[64] H. Sasaki and H. Igarashi, "Topology optimization accelerated by deep learning," *IEEE Transactions on Magnetics*, vol. 55, no. 6, pp. 1-5, June 2019.

[65] S. Baishya, D. Borthakur, R. Kashyap and A. Chatterjee, "A high precision lumped parameter model for piezoelectric energy harvesters," IEEE Sensors Journal, vol. 17, no. 24, pp. 8350-8355, 15 Dec.15, 2017.

[66] G.-Q. Wang and Y.-M. Lu, “An improved lumped parameter model for a piezoelectric energy harvester in transverse vibration,” Shock and Vibration, vol. 2014, pp. 1–12, 2014.

[67] Y. Jung, S. Hong, et al., "Flexible piezoelectric acoustic sensors and machine learning for speech processing", *Advanced Materials*, vol. 32, no. 35, p. 1904020, 2019.

[68] A. Lucas, M. Iliadis, R. Molina and A. K. Katsaggelos, "Using deep neural networks for inverse problems in imaging: beyond analytical methods," *IEEE Signal Processing Magazine*, vol. 35, no. 1, pp. 20-36, Jan. 2018.

[69] K. Shankar, Y. Zhang, Y. Liu, L. Wu and C. Chen, "Hyperparameter tuning deep learning for diabetic retinopathy fundus image classification," *IEEE Access*, vol. 8, pp. 118164 118173, 2020.

[70] T. Kaur and T. K. Gandhi, “Deep convolutional neural networks with transfer learning for automated brain image classification,” *Machine Vision and Applications*, vol. 31, no. 3, 2020.

[71] T. Le, M. T. Vo, T. Kieu, E. Hwang, S. Rho, and S. W. Baik, “Multiple electric energy consumption forecasting using a cluster-based strategy for transfer learning in smart building,” *Sensors*, vol. 20, no. 9, p. 2668, 2020.

[72] H. Shorakaei and A. Shooshtari, "Analytical solution and energy harvesting from nonlinear vibration of an asymmetric bimorph piezoelectric plate and optimizing the plate parameters by genetic algorithm", *Journal of Intelligent Material Systems and Structures*, vol. 29, no. 6, pp. 1120-1138, 2017.

[73] Y. Liao and J. Liang, “Maximum power, optimal load, and impedance analysis of piezoelectric vibration energy harvesters,” Smart Materials and Structures, vol. 27, no. 7, p. 075053, 2018.

[74] M. Prauzek, J. Konecny, M. Borova, K. Janosova, J. Hlavica, and P. Musilek, “Energy harvesting sources, storage devices and system topologies for environmental wireless sensor networks: A review,” *Sensors*, vol. 18, no. 8, p. 2446, 2018.

[75] G. D. Szarka, B. H. Stark and S. G. Burrow, "Review of power conditioning for kinetic energy harvesting systems," in *IEEE Transactions on Power Electronics*, vol. 27, no. 2, pp. 803-815, Feb. 2012.

[76] Q. Wang, Y. Lu, S. Mishin, Y. Oshmyansky, and D. A. Horsley, “Design, Fabrication, and Characterization of Scandium Aluminum Nitride-Based Piezoelectric Micromachined Ultrasonic Transducers,” Journal of Microelectromechanical Systems, vol. 26, no. 5, pp. 1132–1139, 2017.

[77] X. Huang, C. Zhang, and K. Dai, “A multi-mode broadband vibration energy harvester composed of symmetrically distributed U-shaped cantilever beams,” *Micromachines*, vol. 12, no. 2, p. 203, 2021.

Appendix: Published Papers and Prepared Manuscript

[1] H. E. Chimeh, S. Nabavi, M. A. Janaideh and L. Zhang, "Deep-Learning-Based Optimization for a Low-Frequency Piezoelectric MEMS Energy Harvester," in IEEE Sensors Journal, vol. 21, no. 19, pp. 21330-21341, Oct.1, 2021.

[2] H. E. Chimeh, M. A. Janaideh and L. Zhang, "Transfer Learning for Bistable Piezoelectric MEMS Energy Harvester Design," in *Journal of Microelectromechanical Systems* (submitted-under review)